Research Square

Preprints are preliminary reports that have not undergone peer review.
They should not be considered conclusive, used to inform clinical practice,
or referenced by the media as validated information.

Synergistic Enhancement of Membrane Properties and Methylene Blue Removal through Bis-Chalcone-Functionalized Zeolite Filler

Kabiru Hassan Dahiru
Universiti Sains Malaysia
Melati Khairuddean
Universiti Sains Malaysia
Abdul Latif Ahmad
Universiti Sains Malaysia
Mohd Riduan Jamalludin
Universiti Malaysia Perlis
Siti Khadijah Hubadillah
Universiti Utara Malaysia
Azat Seitkhan
Satbayev University
Budi Hastuti
Sebelas Maret University
Mohamad Izrin Mohamad Esham
Universiti Sains Malaysia
Mohd Ridhwan Adam
mohd.ridhwan@usm.my

Universiti Sains Malaysia

Research Article

Keywords: Mixed matrix membrane, natural zeolite clinoptilolite, bis-chalcone, surface modification, wastewater treatment

Posted Date: November 23rd, 2026

DOI: https://doi.org/10.21203/rs.3.rs-11250017/v1

License: This work is licensed under a Creative Commons Attribution 4.0 International License.
Read Full License

Additional Declarations: No competing interests reported.

Synergistic Enhancement of Membrane Properties and Methylene Blue Removal through Bis-Chalcone-Functionalized Zeolite Filler

Kabiru Hassan Dahiru[a,b], Melati Khairuddean[a], Abdul Latif Ahmad[c], Mohd Riduan Jamalludin[d], Siti Khadijah Hubadillah[e], Azat Seitkhan[f], Budi Hastuti[g], Mohamad Izrin Mohamad Esham[c], Mohd Ridhwan Adam[a*]

[a]*Materials Technology Research Group (MaTReC), School of Chemical Sciences, Universiti Sains Malaysia, 11800 Minden, Penang, Malaysia*

[b]*Department of Chemistry, Federal University Lokoja, 270103 Kogi State, Nigeria*

[c]*School of Chemical Engineering, Engineering Campus, Universiti Sains Malaysia, 14300 Nibong Tebal, Pulau Pinang, Malaysia*

[d] *Faculty of Mechanical Engineering & Technology, Universiti Malaysia Perlis, Kampus Tetap Pauh Putra, 02600, Arau, Perlis*

[e] *School of Technology Management and Logistics Universiti Utara Malaysia*

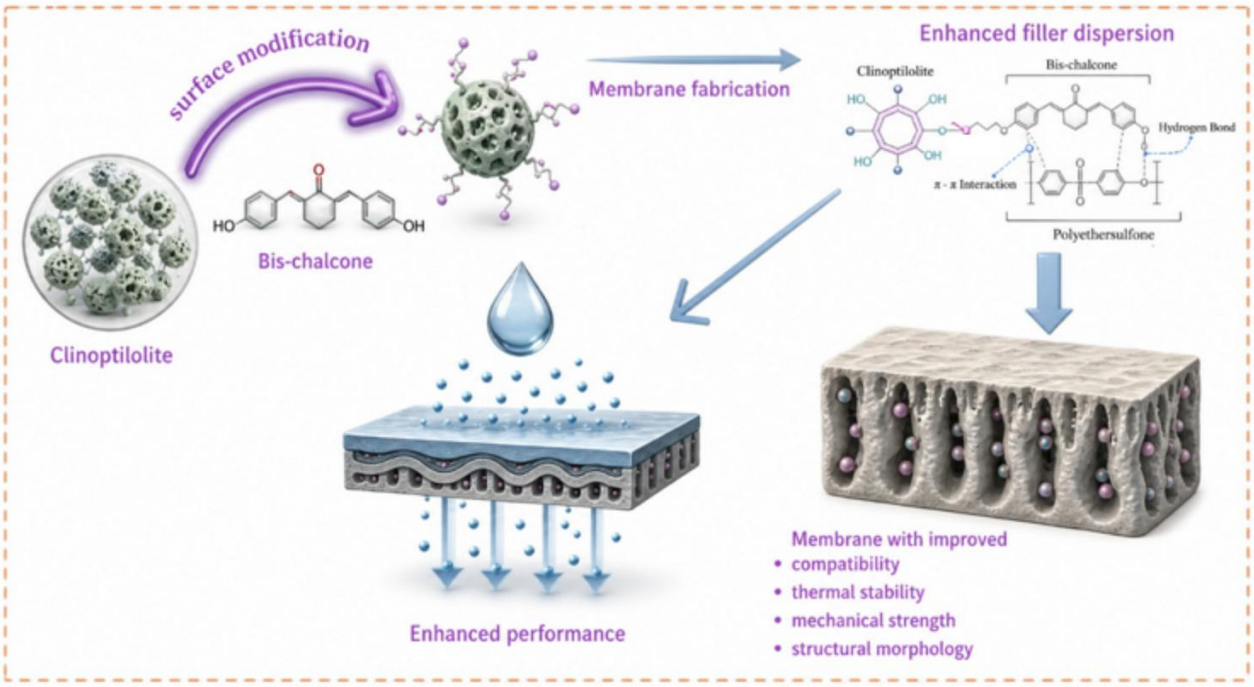
06010 Bukit Kayu Hitam, Changlun, Kedah, Malaysia

[f]*Laboratory of Engineering Profile, Satbayev University, 22 Satbayev Str., Almaty, Kazakhstan*

[e]*Department of Chemistry Education, Faculty of Teacher Training and Education, Universitas Sebelas Maret, Surakarta, Central Java 571 26, Indonesia,*

**Corresponding author: mohd.ridhwan@usm.my*

Graphical abstract



Abstract

Rapid industrialization and population growth have intensified water pollution by discharging wastewater containing dyes, posing serious risks to aquatic systems and human health. Owing to the toxicity and persistence of industrial dyes, their removal before discharge is essential. Membrane filtration offers an effective approach for dye removal. In this study, natural clinoptilolite zeolite (NZ-CLI) was modified with bis-chalcone (DIHYONE) to improve its compatibility with a polyethersulfone (PES) matrix in mixed-matrix membranes (MMMs). Physicochemical analyses using FTIR, BET, TGA, and XRD confirmed modification of the zeolite. The DIHYONE-CLI/PES membranes were evaluated using synthetic methylene blue solutions prepared in deionized water as a model system. Response Surface Methodology (RSM) based on Central Composite Design (CCD) was applied to optimize dye removal and membrane flux. Under optimum conditions of 20 wt.% filler loading, 10.05 mg L^{-1} dye concentration, and pH 8.46, the membrane achieved 98.68% dye removal and a flux of 77.68 $Lm^{-2}h^{-1}$,

compared with the neat membrane, which showed 52.05% and 91.46 $Lm^{-2}h^{-1}$ in dye removal and flux, respectively. This study demonstrates an effective approach for designing organic-inorganic hybrid materials to enhance interfacial compatibility in MMMs and develop efficient adsorptive membranes for targeted contaminant removal in wastewater treatment.

Keywords: *Mixed matrix membrane, natural zeolite clinoptilolite, bis-chalcone, surface modification, wastewater treatment*

1.0 Introduction

The increasing discharge of dye-containing effluents from textile, paper, leather, and plastics industries remains a major water-quality concern. Synthetic dyes can persist in aquatic environments, reduce light penetration, inhibit photosynthetic activity, and increase chemical and biochemical oxygen demand (Bessegato et al., 2019; Imron et al., 2019). Methylene blue (MB), a widely used cationic dye, is frequently selected as a model pollutant because of its high stability, low biodegradability, and potential toxicity to human and aquatic organisms(Ahmadi et al., 2025).

Membrane filtration, adsorption, advanced oxidation, and biological treatment have been widely investigated for dye removal (Pakharuddin et al., 2021; Rathi et al., 2021). Among these approaches, membrane processes offer compact operation, low chemical consumption, and the potential for integration into water-treatment systems (Rathi et al., 2021). However, conventional polymeric membranes may exhibit limited dye removal, susceptibility to fouling, and a trade-off between water permeability and solute retention (Saheed et al., 2026). Incorporating functional inorganic fillers can improve polymeric membranes by modifying their morphology and transport properties and providing adsorption sites that promote contaminant affinity.

Zeolites are promising MMM fillers because of their porous crystalline structure, ion-exchange capacity, thermal stability, and adsorption properties (Hashmi et al., 2026). Clinoptilolite, one of the most abundant natural zeolites, has a relatively high Si/Al ratio and good chemical stability, making it a low-cost candidate for membrane applications (Akyalcin et al., 2026). Nevertheless, direct incorporation of hydrophilic inorganic zeolites into hydrophobic polymer matrices often results in poor filler-polymer compatibility (Song et al., 2025). This

incompatibility can cause particle agglomeration, weak interfacial adhesion, nonselective interfacial voids, and changes in membrane morphology, thereby limiting separation performance (Li et al., 2025).

Surface modification of zeolites is commonly used to improve their compatibility with polymer matrices. Strategies including silane grafting, surfactant treatment, and amine impregnation can introduce organic groups onto the zeolite surface and alter its interfacial behavior (Bahmanzadegan & Ghaemi, 2024a; Chen et al., 2022; Irma et al., 2025). However, some modification methods may provide insufficient interfacial interactions or introduce modifiers that may leach during use (Jusoh et al., 2018). Therefore, there remains a need for surface-engineering approaches that improve zeolite dispersion and adhesion in polymer matrices while retaining functional sites for dye interaction.

In this work, natural clinoptilolite was sequentially functionalized with 3-chloropropyltrimethoxysilane (CPTMS) and the bis-chalcone derivative 2,6-bis(4-hydroxybenzylidene) cyclohexan-1-one (DIHYONE) to produce an organic-inorganic hybrid filler, DIHYONE–CLI. The functionalized filler was incorporated into a polyethersulfone (PES) matrix to fabricate MMMs by phase inversion. The modification was designed to improve filler-polymer compatibility and membrane integrity through interfacial interactions between DIHYONE–CLI and PES, while providing additional adsorption sites that can enhance MB affinity. The membranes were characterized in terms of filler modification, membrane morphology, physicochemical properties, mechanical properties, and filtration performance. The effects of DIHYONE–CLI loading, initial MB concentration, and solution pH on MB removal and permeate flux were subsequently evaluated and optimized using response surface methodology. This study therefore examines bis-chalcone surface modification of clinoptilolite as a route for developing adsorptive PES MMMs for removal of MB from synthetic aqueous solution.

2.0 Materials and Method

2.1 Materials

Polyethersulfone (PES; Ultrason®) was supplied by BASF (Germany). 3-Chloropropyltrimethoxysilane (CPTMS), cyclohexanone, 4-hydroxybenzaldehyde, and DMSO-d_6 were obtained from Acros Organics (India); N-methyl-2-

pyrrolidone (NMP) from R&M Chemicals; toluene and hydrochloric acid from QReC; and methanol and ethanol from Bendosen. Bovine serum albumin (BSA), methylene blue (MB), TLC plates, were obtained from Solarbio Life Sciences, Chemiz, Merck (Germany), and natural clinoptilolite zeolite powder from Shijiazhuang Mining Trade Co., Ltd. (Liaoning, China). All reagents were used as received unless otherwise stated.

2.2 Synthesis of (2, E6E)-2,6-bis[(4-hydroxyphenyl)methylidene]cyclohexan-1-one (DIHYONE)

The bis-chalcone derivative, (2, E6E)-2,6-bis[(4-hydroxyphenyl)methylidene]cyclohexan-1-one (DIHYONE) was synthesized following the method reported by (Abubakar et al., 2024), with minor modifications (Scheme S1). Cyclohexanone (0.125 mL, 1.207 mmol**)** and 4-hydroxybenzaldehyde (0.305g, 2.5 mmol, 2.0 equiv.) were dissolved in methanol (25 mL). A catalytic amount of hydrochloric acid (80%) was added, and the mixture was stirred at room temperature for 24 h. Reaction progress was monitored by thin-layer chromatography. The precipitated product was collected by vacuum filtration, washed with cold methanol, and dried at 60 °C for 24 h to obtain a yellowish-brown solid designated as DIHYONE.

2.3 Two-Step Surface Functionalization of Natural Clinoptilolite

2.3.1 CPTMS functionalization

Natural clinoptilolite (5.0 g) was dried at 70 °C for 24 h and dispersed in toluene (250 mL) with stirring. Subsequently, 3-chloropropyltrimethoxysilane (CPTMS, 6.0 mL) was added, and the suspension was refluxed at 80 °C under continuous stirring for 20 h. During the treatment, CPTMS was expected to undergo hydrolysis and condensation with accessible hydroxyl groups on the clinoptilolite surface, generating a chloropropyl-functionalized surface layer. The solid was recovered by filtration, washed with toluene to remove unreacted silane, and dried at 60 °C overnight. The resulting material was denoted CPTMS-CLI. The proposed surface-functionalization pathway is shown in Scheme S2.

2.3.2 DIHYONE functionalization

CPTMS–CLI (1.8 g) and DIHYONE (0.2 g) were combined at a DIHYONE: CPTMS–CLI mass ratio of 10:90 in ethanol (50 mL). The mixture was stirred under reflux at 80 °C for 24 h. After cooling to room temperature, the solid was recovered by filtration, washed repeatedly with ethanol to remove non-immobilized DIHYONE, and dried at 50 °C for 24 h. The resulting bis-chalcone-functionalized clinoptilolite was denoted DIHYONE-CLI and stored in a sealed container until needed for membrane fabrication

2.4 Membrane Fabrication

Flat sheet mixed-matrix membranes (MMMs) were prepared by dry–wet phase inversion. Neat PES membranes and NZ-CLI/PES and DIHYONE-CLI/PES MMMs containing 5- 30 wt.% filler were fabricated. Filler quantities were calculated using Equation 1. Before use, PES was dried at 60 °C for 24 h. Each filler was dispersed in N-methyl-2-pyrrolidone (NMP) by stirring at 3 70 °C for 1 h. PES was then added to the dispersion to obtain a dope solution containing 18 wt.% PES. The mixture was stirred at 70 °C for 24 h to obtain a homogeneous dope solution. The dope solution was sonicated for I h followed by degassing for another 1 h to remove air bubbles.

The dope solution was cast onto a clean glass plate using a semi-automatic casting machine fitted with a 150 μm casting knife. Casting was performed at 25 °C and 70% relative humidity. After a 30 s air-exposure period, the cast film was immersed in a distilled-water coagulation bath at 25 °C to induce phase inversion. The resulting membranes were soaked in fresh distilled water for 24 h, with periodic water replacement to remove residual NMP. Membranes were stored in distilled water until filtration testing. For dry-state characterization, membranes were dried at room temperature for 24 h. The filler loading was calculated using Equation 1:

$$Filler\ loading\ (wt.\%) = \frac{m_F}{m_F + m_P}\ x\ 100 \qquad \textit{Equation 1}$$

Where m_F and m_p are the masses of filler and polymer, respectively.

2.5 Characterization of pristine and functionalized clinoptilolite

Pristine clinoptilolite (NZ-CLI) and DIHYONE-functionalized clinoptilolite (DIHYONE-CLI) were characterized using techniques such as scanning electron microscopy coupled with energy-dispersive X-ray spectroscopy (SEM-EDX), Fourier-transform infrared spectroscopy (FTIR), X-ray diffraction (XRD), nitrogen adsorption–desorption analysis, and zeta-potential measurements. SEM-EDX was used to evaluate particle morphology and elemental composition, whereas FTIR and XRD were used to assess surface functionalization and preservation of the clinoptilolite framework. Textural properties were determined from nitrogen adsorption–desorption isotherms using BET and BJH methods. Zeta potential was measured over the pH range 2-11 to evaluate changes in surface charge following CPTMS and DIHYONE modifications. Triplicate measurements were conducted at 25 °C, and values are reported as mean ± standard deviation.

2.6 Membrane Characterization

2.6.1 Chemical structure

Fourier-transform infrared (FTIR) spectra of neat PES, NZ-CLI/PES, and DIHYONE–CLI/PES membranes were recorded using a PerkinElmer Spectrum spectrometer over the wavenumber range of 4000–400 cm^{-1} using ATR mode to identify functional groups associated with PES and filler incorporation.

2.6.2 Morphology and Surface Roughness

The surface and cross-sectional morphologies of the membranes were examined using scanning electron microscopy (SEM; Hitachi TM300, Japan). Membrane cross-sections were prepared by cryo-fracturing samples in liquid nitrogen and samples were dried and gold-coated before imaging**.**

Surface topography was examined by atomic force microscopy (AFM; Dimension Edge, Bruker, USA) in tapping mode over a scan area of 10 μm x 10 μm. The arithmetic mean roughness R_a and root-mean-square roughness R_q were determined using Nanoscope Analysis software (Bruker). Measurements were performed at randomly selected locations for each membrane.

2.6.3 Thermal Properties

Thermal stability was evaluated by thermogravimetric analysis (TGA) using PerkinElmer Thermogravimetric Analyzer TGA 8000. Samples were heated from 35 to 800 °C at a heating rate of 10 °C min^{-1} under a nitrogen atmosphere. The onset degradation temperature and residual mass were obtained from the thermogravimetric curves.

2.6.4 Mechanical Properties

Uniaxial tensile testing was used to measure the mechanical properties using a T.XT.plus texture analyzer (Stable Micro Systems, UK) equipped with a 5 kg load cell. Dried membrane strips (50 mm x 10 mm) with a thickness of 0.15 mm were tested according to ASTM D882. 5 specimens were tested for each membrane sample, and Young's modulus was calculated from the initial linear region of the stress-strain curve. Tensile strength and elongation at break were evaluated from the maximum stress and strain at failure, respectively.

2.6.5 Wettability

Membrane wettability was evaluated from the static water contact angle using the sessile-drop method with a water contact-angle analyzer (Rame-Hart Instrument Co., USA). A 0.5 μL droplet of distilled water was placed on the membrane surface, and the contact angle was measured at five randomly selected positions per membrane.

2.6.6 Porosity

Membrane porosity was determined gravimetrically using n-butanol as the wetting liquid. The dried membrane samples of approximately 2 cm x 2 cm were weighed in the dry state (W_d), immersed in n-butanol for 24 h at room temperature, gently blotted with tissue paper to remove excess surface liquid, and reweighed (W_w). The membranes' porosity was calculated according to Equation 2:

$$\varepsilon = \frac{\frac{(W_w - W_d)}{\rho_b}}{\left(\frac{W_w - W_d}{\rho_b}\right) + \frac{W_d}{\rho_{PES}}} \times 100 \qquad \textit{E}\text{quation 2}$$

Where ε is the porosity, Ww is the weight of the membrane, W_d is the weight of the dry membrane, ρ_b is the density of butanol, and ρ_{PES} is the density of PES.

2.7 Membrane Filtration Performance

2.7.1 Pure-Water Flux

Pure-water flux was measured using a laboratory-scale cross-flow filtration system equipped with a circular membrane module of effective area 4.8 cm^2. Before measurement, membranes were compacted using distilled water at 2 bar for 30 min. The pressure was then reduced to 1 bar, and permeate was collected at 5 min intervals for 30 min. The flux (J) was calculated using Equation 3:

$$J = \frac{V}{A.t} \qquad \textit{Equation 3}$$

Where J is flux (L m^{-2} h^{-1}), V is the volume of permeate (L), A is the active surface area of the membrane (m^2), and t is the permeate collecting time (h). Flux is reported in L $m^{-2}h^{-1}$.

2.7.2 Methylene Blue Filtration

MB filtration experiments were conducted using the same cross-flow system. A 1000 mL synthetic MB solution of 10 mg L^{-1} was filtered at a transmembrane pressure of 1 bar, with cross-flow rate maintained at 400 mL min^{-1}. MB concentrations in feed and permeate samples were determined using a UV–visible spectrophotometer at 664 nm. A calibration curve covering the tested concentration range was prepared before analysis. MB removal efficiency was calculated using Equation 4:

$$Removal\ (\%) = \frac{C_f - C_p}{C_f}\ x\ 100 \qquad \textit{Equation 4}$$

Where C_f and C_p are the MB concentrations in the feed and permeate, respectively.

2.8 Antifouling Performance

The antifouling performance of the fabricated membranes was evaluated using 100 mg L^{-1} bovine serum albumin (BSA)as a model protein foulant in a three-stage cross-flow filtration cycle. Before each experiment, membranes

were compacted with deionized water at 2.0 bar for 30 min to obtain a stable permeate flux. In the first stage, the initial pure-water flux (J_{w1}) was measured at 0.5 bar for 30 min, with permeate collected at 5 min intervals. In the second stage, the feed was replaced with the BSA solution, and filtration was conducted under the same cross-flow conditions. The BSA permeate flux (J_{BSA}) was recorded at 5 min intervals. After BSA filtration, the membrane was cleaned using forward rinsing under cross-flow with distilled water for 20 min and a TMP of 1 bar. In the final stage, the recovered pure-water flux (J_{w2}) was measured at 0.5 bar for 30 min.

The Flux Recovery Ratio (FRR) and various fouling resistance ratios, such as total fouling (Rt), reversible Fouling (Rr), and irreversible Fouling (Rirr), were determined according to the equations below.

$$R_r(\%) = \left(\frac{J_{w_2} - J_{BSA}}{J_{w_1}}\right) \times 100 \qquad \textit{Equation 5}$$

$$R_{ir}(\%) = \left(\frac{J_{w_1} - J_{w_2}}{J_{w_1}}\right) \times 100 \qquad \textit{Equation 6}$$

$$FRR\ (\%) = \left(\frac{J_{w_2}}{J_{w_1}}\right) \times 100 \qquad \textit{Equation 7}$$

$$R_t(\%) = R_r + R_{ir} \qquad \textit{Equation 8}$$

2.9 Response Surface Methodology

Response surface methodology (RSM) was applied using Design-Expert software (version 13, Stat-Ease Inc., Minneapolis, MN, USA) to evaluate and optimize the effects of membrane filler loading, initial methylene blue (MB) concentration, and solution pH on MB removal and membrane permeate flux. A central composite design (CCD) comprising 20 experimental runs was employed. The three independent factors were filler loading (A, 10-20 wt.%), initial MB concentration (B, 5-15 mg L^{-1}), and solution pH (C, 4-10). The corresponding coded and actual factor levels are presented in Table 1. The response variables were MB removal (%) and permeate flux (L m^{-2} h^{-1}). A second-order polynomial model was fitted to each response to assess the linear, interaction, and quadratic effects of the independent factors, as expressed in Equation 9:

$$Y = \beta_o + \sum_{i=1}^{k} \beta_i X_i \sum_{i=1}^{k} \beta_{ii} X_i^2 + \sum_{i<j}^{k} B_{ij} X_i X_j + \varepsilon \qquad \textit{Equation 9}$$

Where Y is the predicted response; X_i and X_j are the coded independent variables; β_0 is the intercept; β_i, β_{ii}, and β_{ij} are the linear, quadratic, and interaction coefficients, respectively; and ε represents the residual error. The adequacy of the fitted models was evaluated by analysis of variance (ANOVA), including model significance, lack-of-fit, coefficient of determination (R^2), adjusted R^2, predicted R^2, and residual diagnostics. Numerical optimization was performed to maximize MB removal while maintaining high permeate flux.

Table 1 Experimental factors and coded levels used in the central composite design

Factor	Symbol	Unit	Low level	Center level	High level
Filler loading	A	wt. %	10	15	20
Initial MB concentration	B	mg L^{-1}	5	10	15
Solution pH	C		4	7	10

2.10 Model Validation

Following numerical optimization, the predictive capability of the fitted RSM models was validated experimentally at the optimum conditions identified by Design-Expert software; 20 wt. % DIHYONE-CLI loading, an initial MB concentration of 10.05 mg L^{-1}, and pH 8.46. Six independent validation experiments were performed under these conditions. The experimental MB removal and permeate-flux values were compared with the corresponding model predictions. The percentage relative error between experimental and predicted responses was calculated using Equation 10.

$$Relative\ error = \frac{Actual\ value - Predicted\ value}{Actual\ value} \times 100 \qquad \textit{Equation 10}$$

2.11 Regeneration and Reusability

Regeneration and reusability of the 20 wt.% DIHYONE–CLI/PES membrane was assessed over five consecutive MB filtration–regeneration cycles. Before testing, the membrane was compacted with distilled water at 1 bar for 30 min, or until the permeate flux stabilized. Each cycle used fresh 10 mg L^{-1} MB solution in a cross-flow system at room temperature and 1 bar for 60 min. Following each filtration cycle, the feed tank and membrane module were rinsed with distilled water. The membrane was regenerated in situ by circulating 2% (w/v) $CaCl_2$ in ethanol/water (30:70, v/v) for 30 min under the same hydrodynamic conditions, followed by thorough water rinsing with a 10 min distilled-water circulation step. The sequence was repeated for 5 cycles, and reusability was evaluated by assessing MB removal and permeate flux after each cycle.

3.0 Results and Discussion

3.1 Physicochemical properties of the Filler materials

The morphology of the materials was analyzed using scanning electron microscopy (SEM). The pristine clinoptilolite (NZ-CLI) exhibits irregularly shaped particles with rough, uneven surfaces, consisting of fine grains and larger agglomerates (Fig. 1a). This heterogeneous structure suggests the presence of pores and cavities of varying sizes, thereby increasing surface area. The observed morphology agrees with the reported SEM characteristics of clinoptilolite (Alsuhybani et al., 2026; Özel et al., 2021).

SEM analysis of bis-chalcone-functionalized clinoptilolite (DIHYONE-CLI) in Fig.1b shows a distinct organic overlayer on the zeolite surface, suggesting successful functionalization. The uniform coating indicates a change in surface appearance consistent with deposition of an organic-containing surface layer. Importantly, particle size and morphology remain largely unchanged after modification, suggesting that the modification is on the surface and does not affect the zeolite framework (Wang et al., 2018). This approach preserves the intrinsic structure of clinoptilolite while introducing functional organic groups that can improve compatibility in membrane fabrication.

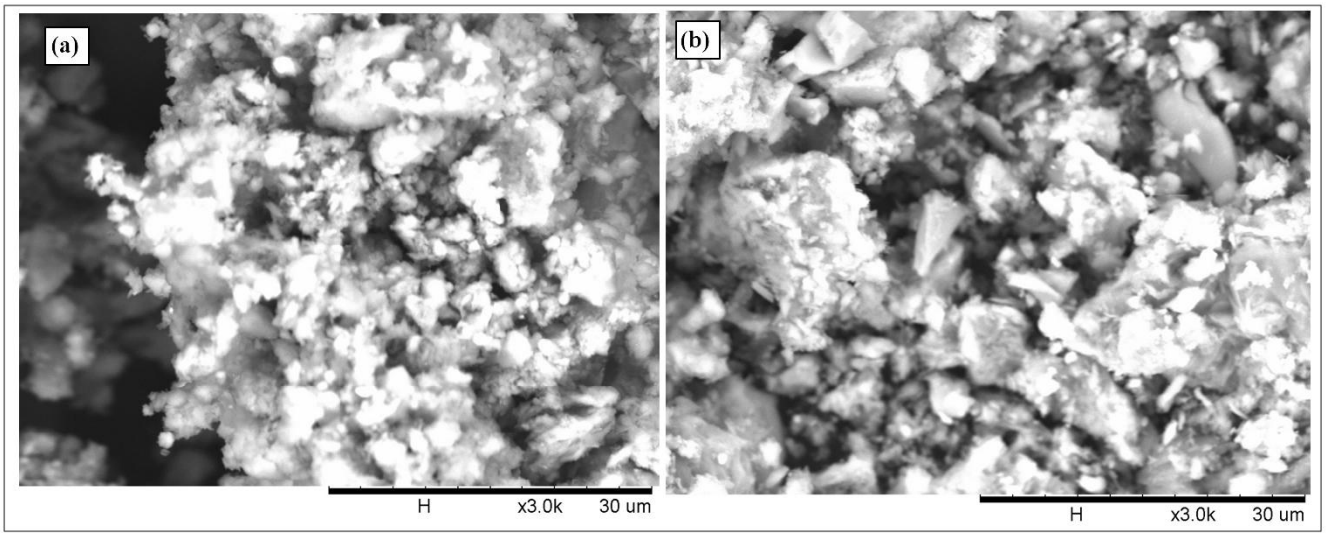


Fig. 1 SEM image of (a) NZ-CLI, and (b) DIHYONE-CLI

The elemental composition of pristine clinoptilolite (NZ-CLI) was evaluated by EDX spectroscopy (Table 2). Oxygen, silicon, and aluminum were the principal detected elements, with contents of 47.62, 32.17, and 7.99 wt.%, respectively, confirming the aluminosilicate character of the material. Minor amounts of Ca, Mg, and Fe were also detected, consistent with the compositional heterogeneity typically observed in natural clinoptilolite(Cechinel et al., 2016; de Lima et al., 2021; Sáez et al., 2021).

Table 2 Elemental composition of NZ-CLI and DIHYONE-CLI

Sample	O	Si	Al	Ca	Fe	Mg	Na	Cl	C
NZ-CLI	47.62	32.17	7.99	6.29	4.84	1.09	ND	ND	ND
DIHYONE-CLI	31	24	4.27	0	ND	0.73	0.22	4.28	35.5

*All elemental values are reported in wt.%. ND: not detected

Surface functionalization produced substantial changes in the EDX composition of clinoptilolite (Table 2). In DIHYONE-CLI, the relative contributions of the aluminosilicate framework elements decreased, with O, Si, and Al decreasing from 47.62, 32.17, and 7.99 wt.% in NZ-CLI to 31.00, 24.00, and 4.27 wt.%, respectively. In contrast, DIHYONE-CLI exhibited a substantial carbon signal (35.50 wt.%) and detectable chlorine (4.28 wt.%), which were

absent in NZ-CLI. These compositional changes are consistent with the presence of organic and chloropropyl moieties after the CPTMS and DIHYONE treatment. (Lu et al., 2023).

Fig. 2a shows the XRD patterns of unmodified clinoptilolite (NZ-CLI) and DIHYONE-functionalized clinoptilolite (DIHYONE-CLI). Both samples exhibit the characteristic reflections of clinoptilolite at 2θ values of approximately 9.82°, 11.15°, 22.40°, 26.62°, 27.85°, 29.98°, and 31.96°. The retention of these diffraction peaks after functionalization indicates that the crystalline clinoptilolite phase was preserved and that the treatment did not induce major detectable changes in the zeolite crystal structure. The absence of distinct additional crystalline reflections attributable to the modifier is consistent with the low loading and/or noncrystalline distribution of the clinoptilolite surface (Ambrožová et al., 2017; Dikić et al., 2013; Mortazavi et al., 2021; Nizam et al., 2021).

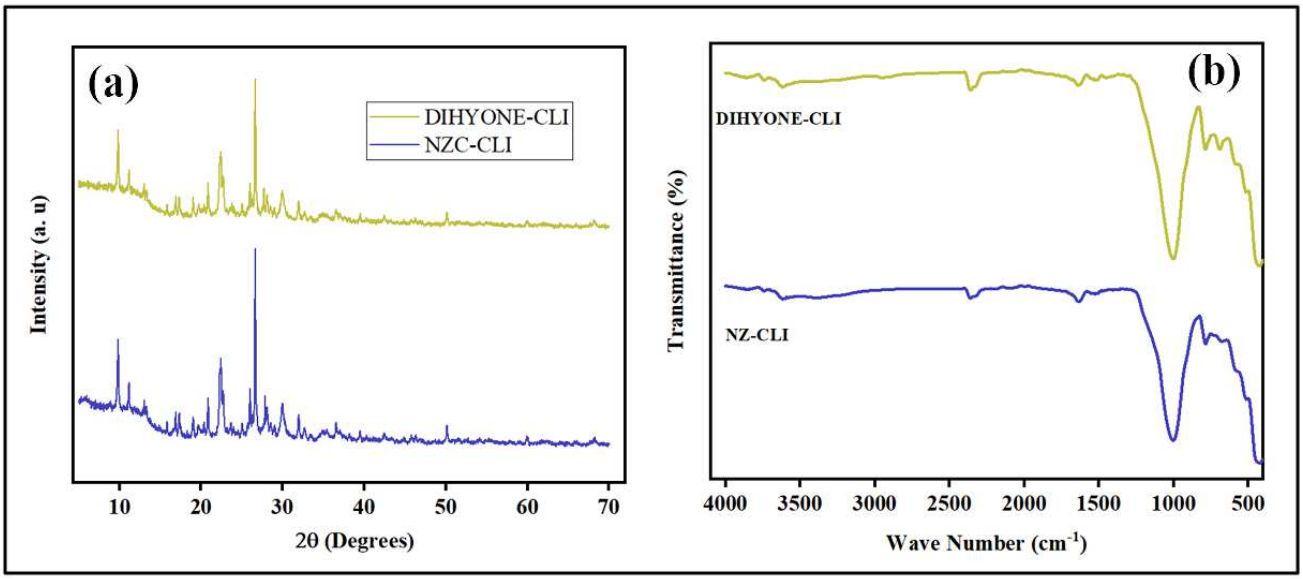


Fig. 2 (a) XRD pattern and (b) FTIR spectrum for NZ-CLI and DIHYONE-CLI

The FTIR spectrum of pristine clinoptilolite (NZ–CLI) (Fig. 2b) exhibited a broad band at approximately 3624 cm^{-1} and a band near 1646 cm^{-1}, assigned to the stretching and bending vibrations of hydroxyl groups and adsorbed or structural water, respectively. The intense band at approximately 1013 cm^{-1} was attributed to asymmetric stretching vibrations of T-O-T linkages $(T, = SiAl)$in the aluminosilicate framework. A further band near 793 cm^{-1} was

assigned to symmetric T-O-T vibrations, consistent with clinoptilolite (Postole et al., 2025). DIHYONE-CLI retained the characteristic clinoptilolite framework bands, consistent with the XRD results indicating preserved crystallinity after modification. In addition, a band near 2850 cm^{-1} appeared in the DIHYONE–CLI spectrum and was assigned to aliphatic C-H stretching vibrations associated with the CPTMS and/or DIHYONE organic components. The absence of major changes in the aluminosilicate framework bands indicates that the modification did not cause significant disruption of the clinoptilolite structure (Shi et al., 2023).

Figure 3 presents the nitrogen adsorption-desorption isotherms of NZ-CLI and DIHYONE-CLI. Both samples display nearly identical adsorption and desorption profiles, which suggests similar surface properties. The lack of a limiting adsorption plateau and the marked increase in nitrogen uptake as P/P_o approaches unity indicate adsorption within interparticle voids and incompletely filled mesopores or macropores, characteristic of a 3H-type hysteresis loop (Restiawaty et al., 2024). The hysteresis observed at intermediate to high relative pressures aligns with capillary condensation in slit-like pores or voids formed between aggregated clinoptilolite particles (Grifasi et al., 2026). DIHYONE-CLI exhibits a slightly different nitrogen uptake, implying that surface modification has altered the accessibility or arrangement of certain interparticle pores (Dionisiou & Matsi, 2024).

Surface functionalization substantially altered the textural properties of clinoptilolite (Table 3). The BET surface area decreased from 22.24 m^2g^{-1} to 6.76 m^2g^{-1} following organic surface modification, while the total pore volume declined slightly from 0.0634 cm^3g^{-1} to 0.0613 cm^3g^{-1}. The average pore size also decreased from 13.72 nm to 9.80 nm, which indicates partial pore blockage by the grafted organic moieties (Dimitrijević et al., 2025). The pore-size distribution profiles in Figure 3 (c-d) confirm that most pores remain within the mesoporous range (2–50 nm), suggesting that the modification primarily affected the external surface of the zeolite rather than its framework porosity (Naito et al., 2018).

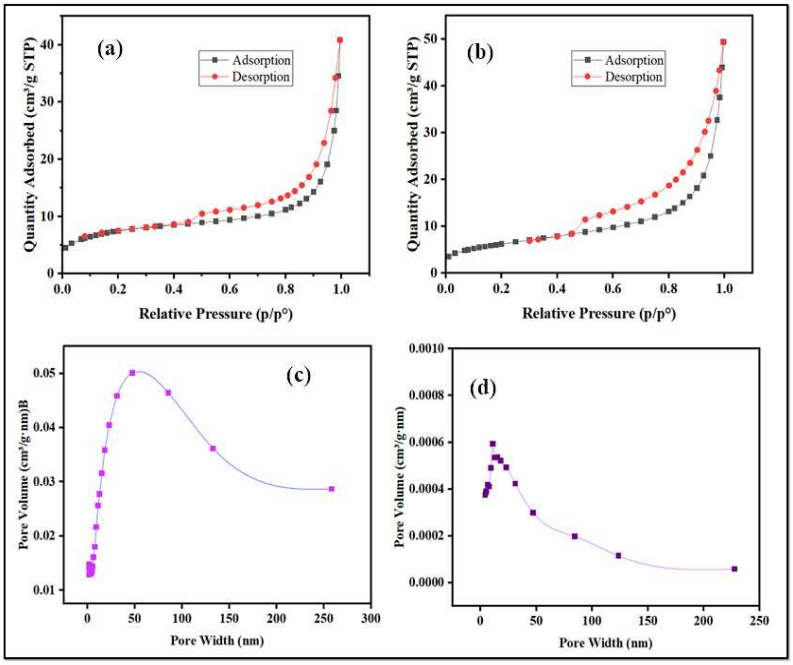


Fig. 3 Nitrogen adsorption–desorption isotherms of (a) NZ-CLI and (b) DIHYONE-CLI, and pore-size distributions of (c) NZ-CLI and (d) DIHYONE-CLI.

Table 3 Textural properties of NZ-CLI and DIHYONE-LI

Material	BET Surface Area (m2/g)	Total Pore Volume (cm3/g)	Average Pore size (nm)
NZ-CLI	22.2412	0.0634	13.7294
DIHYONE-CLI	6.7563	0.06130	9.7951

Figure 4 displays the thermogravimetric analysis (TGA) profiles of NZ-CLI and DIHYONE-CLI. Both samples demonstrate minor mass loss below approximately 150 °C, which is attributed to the desorption of physically adsorbed water, a characteristic feature of hydrated zeolitic materials. Subsequently, NZ-CLI exhibits negligible mass loss up to approximately 800 °C, indicating the high thermal stability of the clinoptilolite framework. In contrast, DIHYONE-CLI shows a pronounced mass loss between approximately 200 and 600 °C before achieving

thermal stability near 900 °C. This mass-loss region is ascribed to the thermal decomposition of the grafted organic moieties, providing further evidence of successful clinoptilolite functionalization.

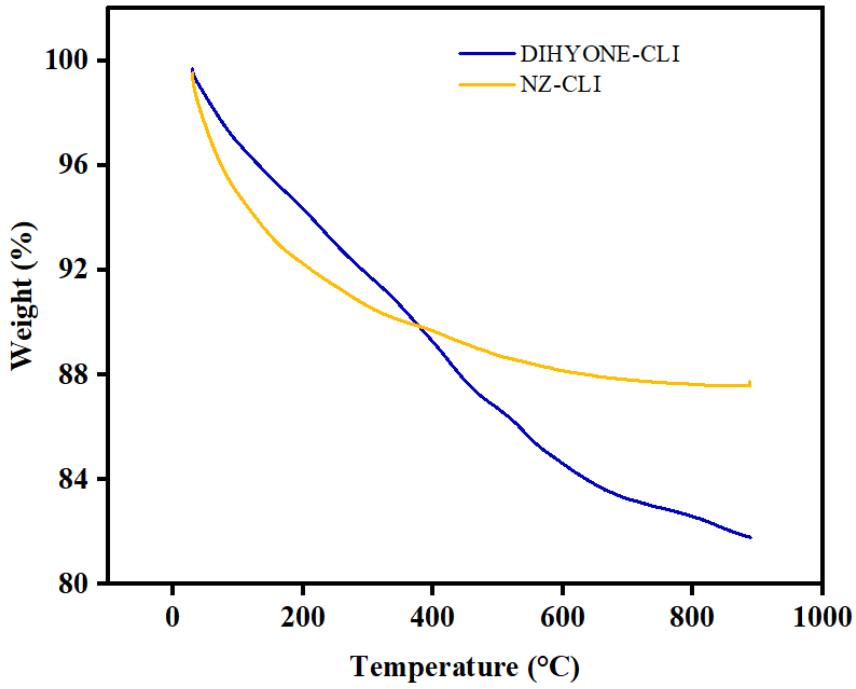
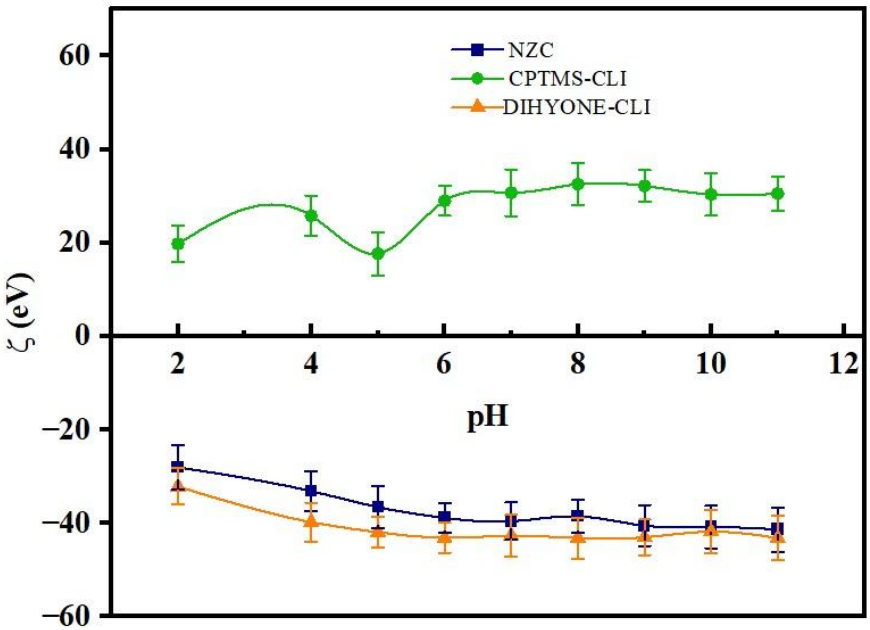


Fig. 4 Thermogram of NZ-CLI and DIHYONE-CLI

Fig. 5 shows the zeta potentials of NZ-CLI, CPTMS-CLI, and DIHYONE–CLI at pH 2-11. NZ–CLI remained negatively charged (-28 to -42mV), whereas CPTMS functionalization shifted the potential to positive values (+19 to +30 mV), confirming substantial modification of the native clinoptilolite surface, consistent with formation of an organosilane-containing surface layer on zeolitic and silica-based surfaces (Han et al., 2020; Męczyńska-Wielgosz et al., 2016; Özel et al., 2021). Subsequent DIHYONE functionalization restored a negative zeta potential (-33 to -43 mV), with more negative values than NZ–CLI under acidic conditions. These sequential charge shifts provide evidence of successful stepwise surface modification. The negative charge of DIHYONE-CLI is also favorable for electrostatic interaction with cationic MB.



1. Fig. *5* Zeta potential of NZ-CLI, CPTMS-CLI and DIHYONE-CLI

3.2 Morphology and physicochemical properties of the membranes

ATR-FTIR spectra of neat, NZ-CLI/PES, and DIHYONE-CLI/PES membranes are shown in Fig. 6. The neat membrane shows a characteristic peak at 1587 cm^{-1}, corresponding to aromatic stretching vibrations. Another notable peak at 1240 cm-^{1} is attributed to symmetric Ar-O-Ar aromatic ether vibrations. A prominent peak at 1150 cm^{-1} corresponds to the characteristic absorption band for asymmetric stretching of the sulfone group (O=S=O) in PES. (Anbealagan et al., 2021). The spectra of the modified membranes differ slightly from those of the neat PES membrane. For the NZ-CLI/PES, the T-O-T (T = Al or Si) vibration band at 1000-1100 cm-1 likely overlaps with the Ar-O-Ar and the O=S=O peaks of the PES. At higher NZ-CLI loadings, a new peak appears at 2300-2500 cm^{-1}. Similarly, DIHYONE-CLI/PES membranes show overlapping peaks with PES, with a new band at 2800-3000 cm^{-1}, which can be attributed to C-H stretching in the CPTMS and DIHYONE units, confirming the successful incorporation of the fillers into the PES matrix.

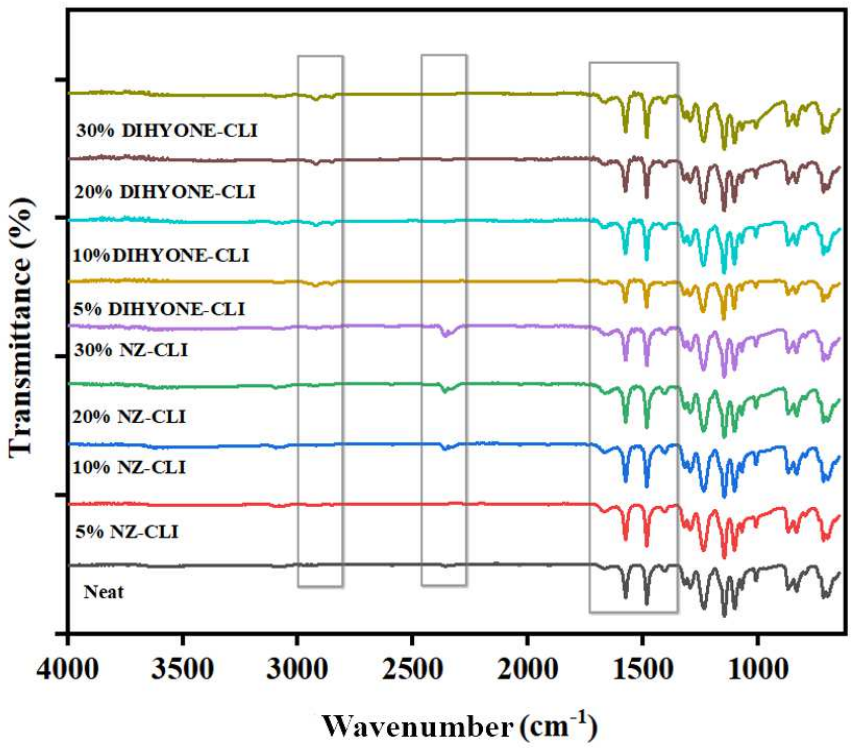


Fig. 6 FTIR spectra of NZ-CLI/PES and DIHYONE-CLI/PES membranes

SEM images (Fig. 7) show the typical asymmetric phase-inversion structure of PES membranes, comprising a relatively dense upper layer and a porous finger-like sublayer. At low to moderate filler loading, both NZ–CLI/PES and DIHYONE–CLI/PES membranes retain this morphology. However, increasing NZ-CLI loading produces localized particle-rich regions, apparent interfacial gaps, and progressive disruption of the finger-like macrovoids, most evident at 30 wt.%. In comparison, DIHYONE–CLI/PES retains a comparatively more continuous finger-like porous structure at equivalent loading. This difference is consistent with improved filler dispersion and polymer-filler compatibility following DIHYONE surface modification, which reduces the tendency of clinoptilolite particles to form large aggregates during membrane formation

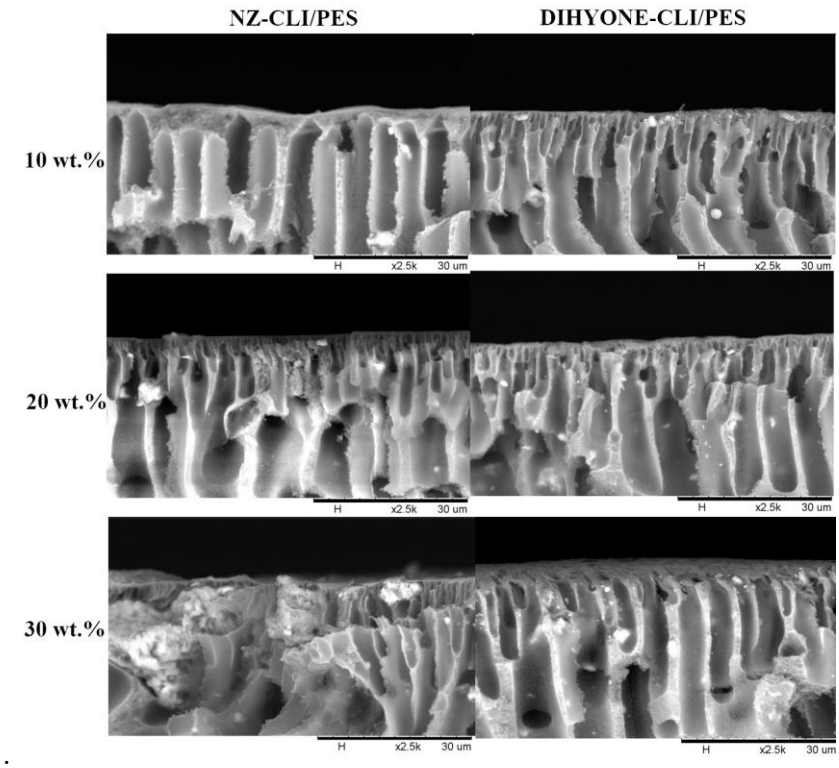


Fig. **7** Representative cross-sectional SEM micrographs of NZ–CLI/PES and DIHYONE–CLI/PES mixed-matrix membranes containing 10, 20, and 30 wt.% filler

Atomic force microscopy (AFM) analysis was conducted in tapping mode over a 1 × 1 μm scan area to evaluate membrane surface morphology (Figure 9).). In the AFM morphology, the darker regions correspond to depressions (pores and valleys), while the brighter regions correspond to elevated features (peaks). The surface roughness properties were quantified by the average (R_a) and root-mean-square (R_q) roughness. Both parameters increased with filler loading, with DIHYONE-CLI/PES membranes exhibiting greater roughness than NZ-CLI/PES membranes at comparable loadings (Table S2). Increased roughness may enhance adsorption by increasing the accessible surface area and active sites (Russo et al., 2021), but may also promote foulant accumulation within surface depressions (Tayeh et al., 2025).

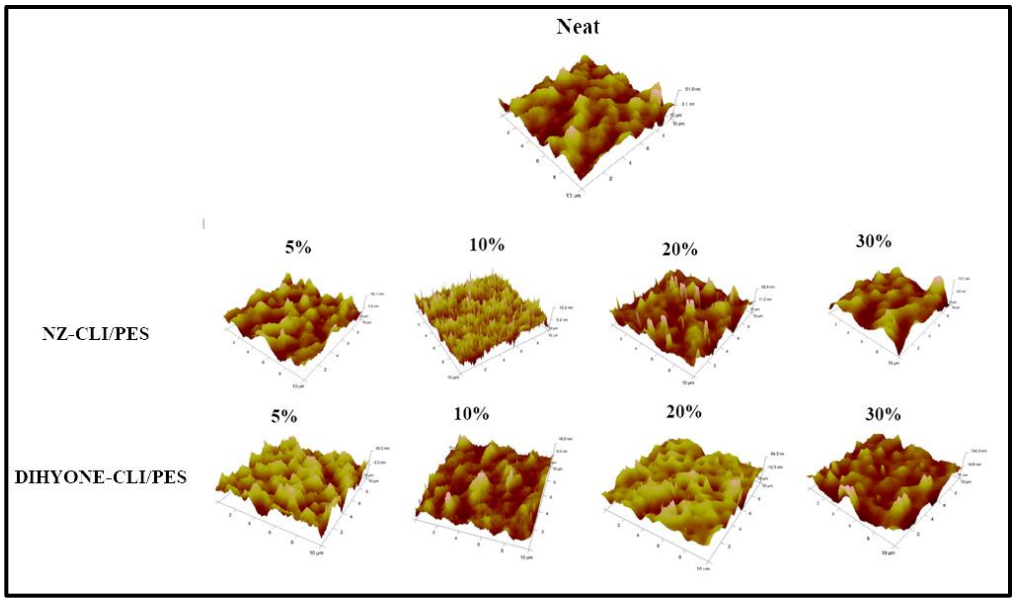


Fig. 8 AFM topography images of neat PES, NZ–CLI/PES, and DIHYONE–CLI/PES membranes at the specified filler loadings.

Fig 9 presents the TGA curves of pristine and modified membranes. Incorporating both fillers shifted the onset degradation temperature to higher values (Table S1), indicating improved thermal properties after filler reinforcement (Cadar et al., 2020; Król et al., 2024). For NZ-CLI/PES membranes, the onset temperature initially increases with lower loadings but declines with higher loadings. This decline may result from filler agglomeration and poor interfacial adhesion, which create thermally sensitive defect regions (Bhiogade & Kannan, 2021). In contrast, DIHYONE-CLI/PES membranes exhibited a consistent increase in onset temperature with increasing filler loading, indicating improved polymer-filler compatibility and restricted chain mobility through enhanced interfacial interactions (Khan et al., 2025; Tian et al., 2020). However, at 30%, the onset temperature slightly decreased, suggesting that thermal stability plateaued beyond the optimal filler concentration (Bhiogade & Kannan, 2021).

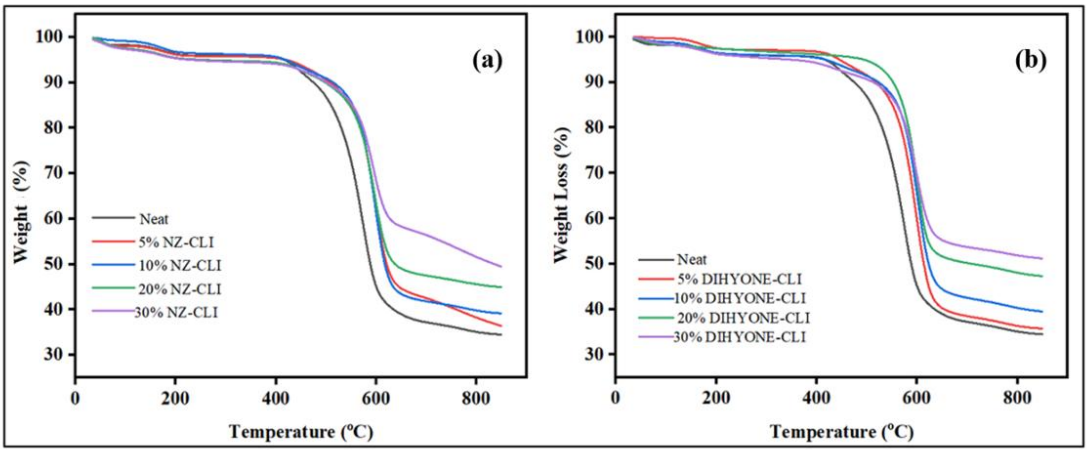


Fig. 9 Thermograms of (a) NZ-CLI/PES and (b) DIHYONE-CLI/PES membranes

The mechanical properties are presentedmposite membranes are presented in Table 4, while the corresponding stress-strain curves are provided in Fig. S3. Membrane formulation significantly affected Young's modulus, tensile strength, and elongation at break ($p < 0.001$). The 20 wt.% DIHYONE-CLI/PES membrane showed the most favorable overall mechanical performance, with the highest Young's modulus (219.38 ± 3.88 MPa), tensile strength (0.1204 ± 0.0123 MPa), and elongation at break (170.90 ± 20.96%). Its modulus and elongation were significantly greater than those of the other formulations, whereas its tensile strength did not differ significantly from those of formulations in the same Tukey group. These results identify 20 wt.% DIHYONE-CLI as the optimum tested loading for balancing stiffness, strength, and ductility. The improvement is consistent with enhanced filler dispersion and polymer-filler stress transfer after surface modification, as supported by the more continuous finger-like substructure observed by SEM (Babapour & Şen, 2024; Rafiee, 2025).

Table 4 Mechanical properties of neat PES and mixed-matrix membranes

Membrane	Young's modulus (MPa)	Tensile strength (MPa)	Elongation at break (%)
Neat	164.11 ± 2.0^{d}	0.0822 ± 0.0159^{abc}	118.958 ± 7.33^{b}
5 wt.% NZ-CLI	163.30 ± 3.55^{d}	0.0400 ± 0.0228^{d}	118.62 ± 13.82^{b}
10 wt.% NZ-CLI	172.29 ± 4.03^{c}	0.0572 ± 0.0324^{cd}	120.44 ± 7.62^{b}
20 wt.% NZ-CLI	183.18 ± 3.24^{b}	0.0934 ± 0.0163^{abc}	125.95 ± 6.50^{b}
30 wt.% NZ-CLI	167.92 ± 3.97^{cd}	0.0744 ± 0.0186^{abc}	124.76 ± 7.16^{b}
5 wt.% DIHYONE-CLI	168.99 ± 2.99^{cd}	0.0920 ± 0.0149^{abc}	119.48 ± 9.13^{b}
10 wt.% DIHYONE-CLI	186.36 ± 3.29^{b}	0.0618 ± 0.0186^{cd}	133.14 ± 12.20^{b}
20 wt.% DIHYONE-CLI	219.38 ± 3.88^{a}	0.1204 ± 0.0123^{a}	170.90 ± 20.96^{a}
30 wt.% DIHYONE-CLI	212.82 ± 3.76^{a}	0.1018 ± 0.0096^{ab}	130.35 ± 10.65^{b}

Values are expressed as mean ± standard deviation (n = 5 membrane samples). Within each column, values sharing at least one superscript letter are not significantly different; values with no shared letters differ significantly at $p < 0.05$, as determined by one-way ANOVA followed by Tukey's HSD test.

Fig. 10 shows the static water-contact angles of neat PES and the composite membranes. Neat PES exhibited a contact angle of 75.8°. Incorporation of NZ-CLI reduced the contact angle to 63.1°at 5 wt.%, consistent with increased surface wettability, likely due to exposure of hydrophilic zeolitic groups. At higher NZ-CLI loadings, the contact angle increased slightly to 67.1-68.3° but remained below that of neat PES. DIHYONE-CLI/PES membranes exhibited higher contact angles than NZ-CLI/PES at equivalent loading, decreasing from 75.4°at 5 wt.% to 71.5°at 30 wt.%. This behavior is consistent with the relatively more hydrophobic organic surface component introduced by DIHYONE modification. Nevertheless, all composite membranes retained water-contact angles below 90°, indicating wettable surfaces. Representative water-droplet images are provided in Fig. S 5.

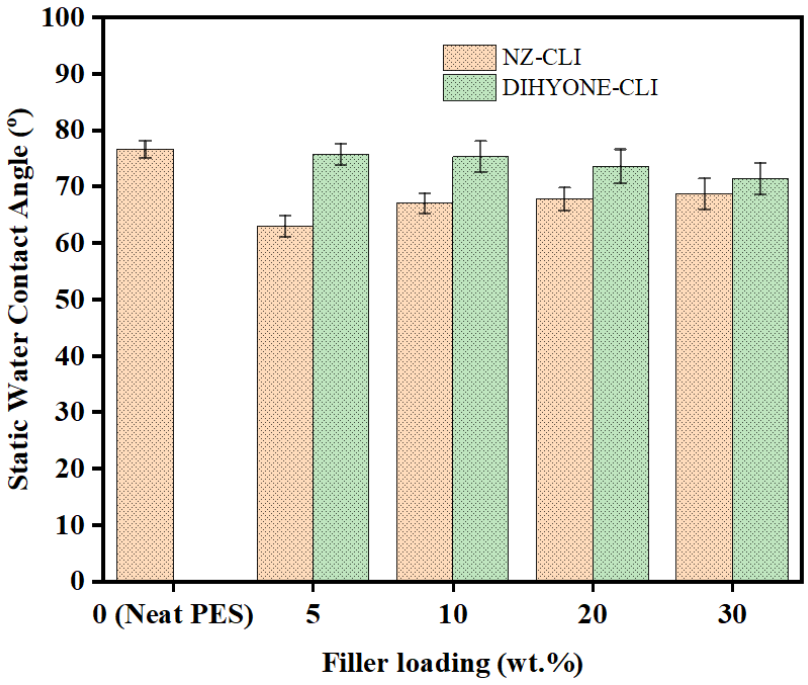


Fig. 10 Water contact angle of NZ-CLI/PES and DIHYONE-CLI/PES membranes. Values are presented as

Gravimetric porosity differed significantly among membrane formulations ($p < 0.00$; Table 5). Neat PES exhibited the highest mean porosity (82.09 ± 4.93%). At 5 and 10 wt.% loading, DIHYONE–CLI/PES retained porosity of 75.89 ± 3.04% and 75.64 ± 0.76%, respectively, none of which differed significantly from neat PES. DIHYONE-CLI/PES showed higher mean porosity than NZ-CLI/PES at similar loadings from 5 to 20 wt.%, consistent with improved filler incorporation during phase inversion. However, these corresponding pairwise differences were not statistically significant. At 30 wt.%, DIHYONE-CLI/PES displayed the lowest porosity (59.43 ± 1.78%), confirming that excessive filler loading causes membrane densification despite surface modification (Almansouri et al., 2024; Zare, 2016).

Table 5 Porosity measurement of Neat PES and composite membranes

Filler Loading (wt.%)	Porosity (%)	
	NZ-CLI/PES	DIHYONE-CLI/PES
Neat	82.09 ± 4.93^{a}	
5	73.74 ± 7.37^{abc}	75.89 ± 3.04^{ab}
10	68.78 ± 4.81^{bcd}	75.64 ± 0.76^{ab}
20	66.33 ± 1.99^{bcd}	$70.76 \pm 4.95a^{bcd}$
30	62.58 ± 3.74^{cd}	59.43 ± 1.78^{d}

Values are presented as mean ± standard deviation (n = 3 membrane samples). Within a column, means sharing at least one superscript letter are not significantly different at $p < 0.05$ according to one-way ANOVA followed by Tukey's HSD test

3.3 Membrane performance

3.3.1 Pure-water flux

Pure-water flux (PWF) results are presented in Fig. 6. Neat PES exhibited a PWF of about 86 L $m^{-2}h^{-1}$. Incorporation of NZ-CLI increased the mean PWF to around 93, 94, and 92 L $m^{-2}h^{-1}$ at 5, 10, and 20 wt.% loading, respectively. This improvement may reflect the hydrophilic nature of clinoptilolite, which can enhance water affinity and facilitate water transport through the membrane (Samanta et al., 2023). In contrast, DIHYONE–CLI/PES membranes showed PWF values broadly comparable to neat PES across the tested loadings, without the increase observed for NZ–CLI/PES. Their comparatively lower flux may be associated with lower bulk porosity and the more hydrophobic organic component introduced during DIHYONE functionalization (Wang et al., 2023). These results indicate that PWF is governed not only by bulk porosity, but also by surface wettability, pore connectivity, and filler-polymer interfacial structure.

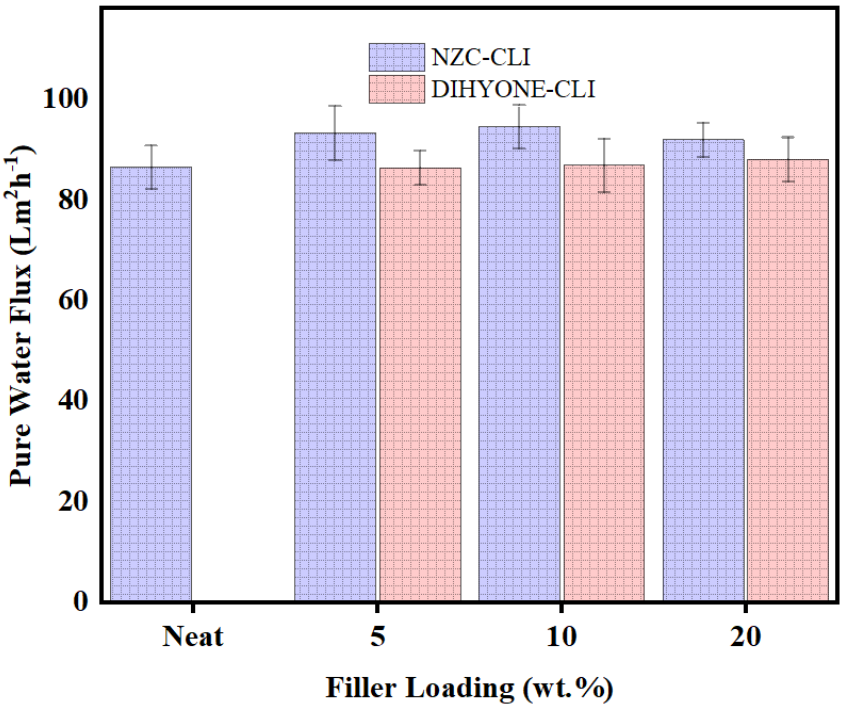


Fig. 11 Pure water flux of Neat, NZ-CLI/PES and DIHYONE-CLI/PES membranes

3.3.2 Membrane antifouling property

The antifouling performance of the membranes was assessed using 100 mg L^{-1} bovine serum albumin (BSA) via time-dependent flux measurements (Fig S6). Pure water flux was recorded for 30 min, followed by 30 min of BSA filtration. Afterward, hydraulic cleaning was performed by forward rinsing under crossflow, and the pure water flux was remeasured to determine fouling ratios and flux recovery. The neat PES membrane exhibited a substantial flux decline during BSA filtration and only partial recovery after cleaning, indicating severe surface fouling and pore blockage. The resulting total fouling ratio (R_t), reversible fouling ratio (R_r), irreversible fouling ratio (R_{ir}), and flux recovery ratio (FRR) are presented in Fig. 7. Neat PES exhibited the greatest flux decline during BSA filtration, showing the poorest antifouling behavior, with R_t, R_r, and R_{ir} values of 55.77%, 31.61%, and 24.12%, respectively, and an FRR of approximately 76%. This indicates substantial BSA deposition and incomplete flux recovery after hydraulic cleaning.

Adding NZ-CLI markedly improved antifouling performance. The 5 and 10 wt.% NZ-CLI/PES membranes showed low total and irreversible fouling and high FRRs of approximately 99% and 96%, respectively. The 10 wt.% membrane had the lowest total fouling, approximately 6%. At 20–30 wt.% loading, total and irreversible fouling increased, and FRR decreased, indicating that excessive NZ-CLI loading may compromise surface uniformity or pore accessibility.

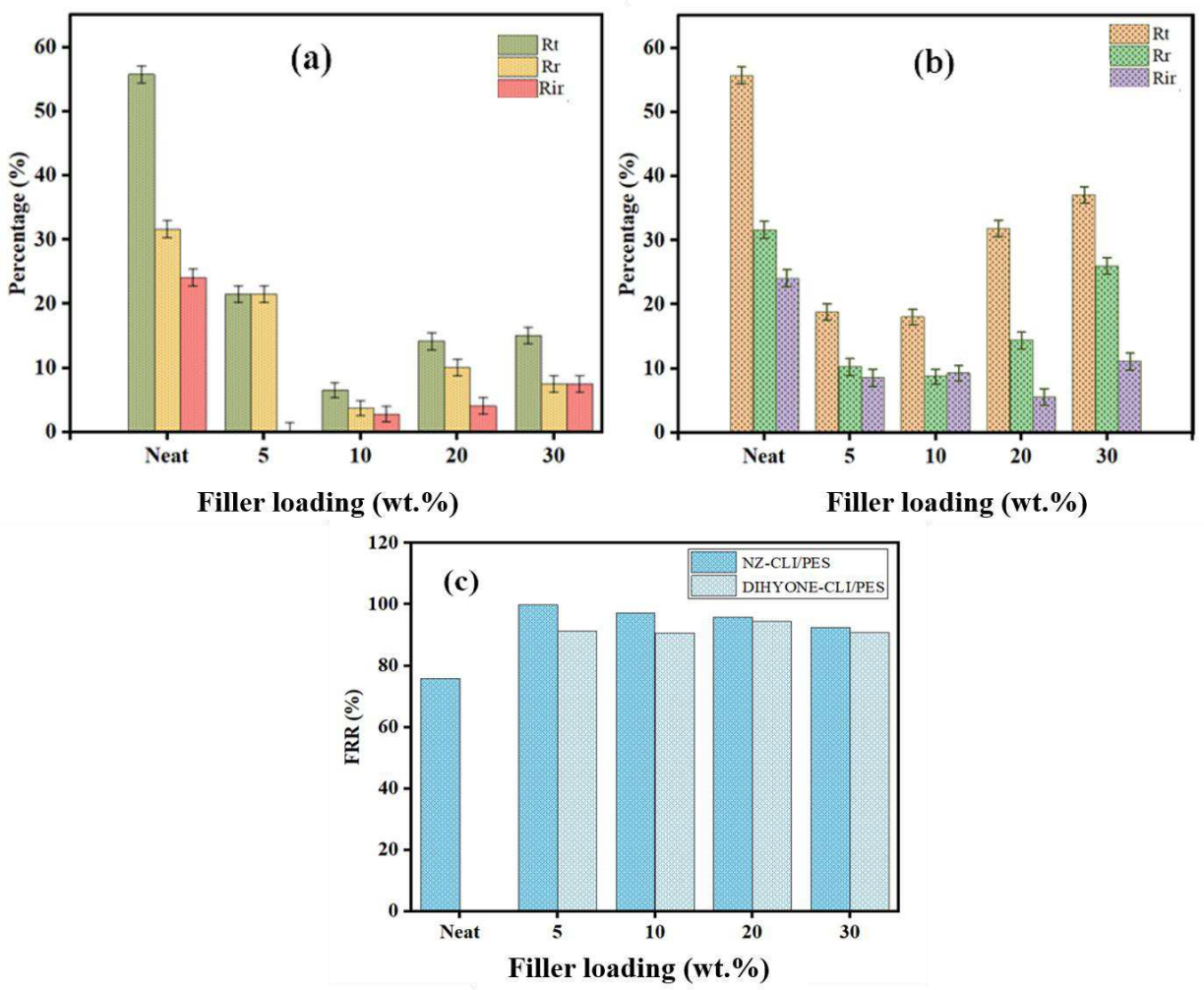


Fig 12 Fouling resistance properties (a) of NZ-CLI/PES and (b) DIHYONE-CLI/PES membranes, and (c) FRR of the NZ-CLI/PES and DIHYONE-CLI/PES membranes

DIHYONE-CLI/PES membranes also displayed more favorable antifouling metrics than neat PES, with the lowest total fouling at 10 wt.%, while the highest FRR was observed at 20 wt.%. However, at 5 and 10 wt.%, DIHYONE-CLI/PES had higher fouling and lower FRR than the corresponding NZ-CLI/PES membranes. The modification therefore did not consistently improve BSA resistance at low loading, possibly because its altered surface chemistry partly offsets the antifouling benefit of the zeolite. At 20 wt.%, DIHYONE-CLI/PES showed lower fouling and better recovery than NZ-CLI/PES, suggesting a potential benefit of modification at intermediate loading. These results show that, 5-10 wt.% NZ-CLI/PES provided the best BSA antifouling performance, whereas DIHYONE modification was most beneficial at 20 wt.% loading. The results indicate that fouling resistance is controlled by filler loading, dispersion, surface chemistry, and membrane structure rather than filler content alone.

3.3.3 Methylene blue ultrafiltration performance

Fig. 13 presents the preliminary ultrafiltration performance of neat PES and DIHYONE-CLI/PES membranes for MB removal. Neat PES showed the lowest dye removal, at approximately 52%, despite the highest flux of approximately 92 L m^2 h^{-1}. Incorporation of DIHYONE-CLI increased dye removal to approximately 74%, 85%, and 92% at 5, 10, and 20 wt.% loading, respectively. This improvement was accompanied by a progressive reduction in flux, from approximately 88 L m2 h^{-1} at 5 wt.% to 76 L m2 h^{-1} at 20 wt.%, indicating a trade-off between dye removal and hydraulic permeability.

The improved MB removal with DIHYONE-CLI loading is consistent with a greater abundance of adsorption sites in the modified zeolite. Because MB is a cationic dye, electrostatic attraction to negatively charged clinoptilolite surfaces may promote dye uptake. DIHYONE functionalization may also contribute additional interactions, such as π-π interactions and hydrogen bonding. However, since molecular-weight cut-off and pore-size distribution were not determined, the relative contributions of adsorption and size exclusion cannot be quantified. It is therefore more accurate to state that MB removal likely results from combined adsorption and membrane-filtration effects, with adsorption plausibly making a substantial contribution (Fitri et al., 2025).

At 30 wt.% DIHYONE-CLI, dye removal declined to approximately 74% and flux decreased markedly to approximately 55 L m^{-2} h^{-1}. This loss of performance suggests that excessive filler loading may cause agglomeration, partial pore blockage, increased transport resistance, or reduced accessibility of adsorption sites. Therefore, 20 wt.% DIHYONE-CLI/PES achieved the most favorable preliminary balance between MB removal and permeate flux.

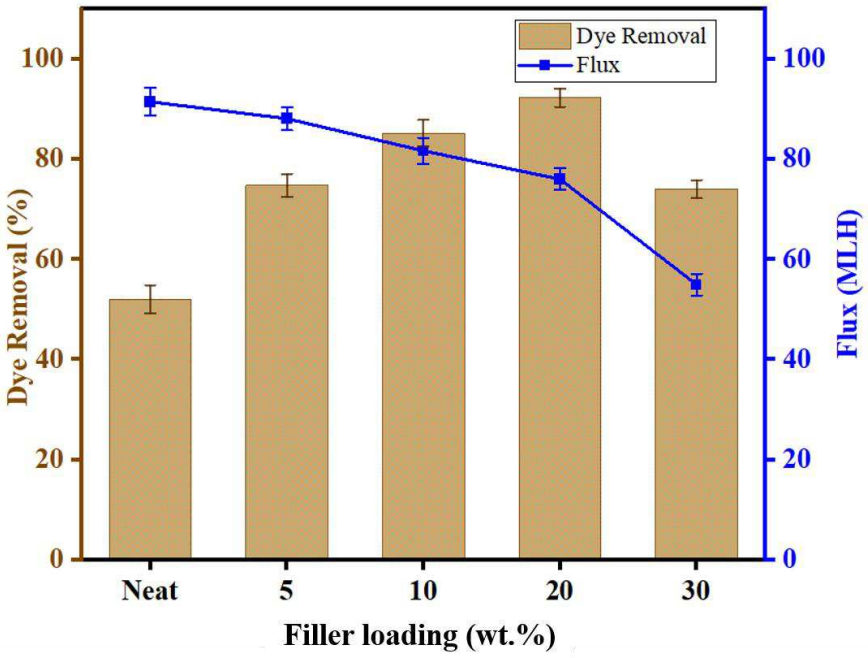


Fig. 13 Preliminary MB removal and permeate flux study

3.4 Optimization of the membrane performance

Response surface methodology (RSM) coupled with a central composite design (CCD) was used to model and optimize methylene blue (MB) removal and membrane flux during ultrafiltration. Filler loading (A), dye concentration (B), and solution pH (C) were selected as independent variables. The CCD generated 20 experimental runs to evaluate the linear, interaction, and quadratic effects of these variables. The experimental design and response data are summarized in Table 6.

Table 6 CCD design matrix and experimental responses (dye removal and membrane flux)

Std	Run	A: Filler Loading (wt.%)	B: Dye Concentration (mg L^{-1})	C: pH	Dye Removal (%)	Flux (L $m^{-2}h^{-1}$)
15	1	15	10	7	94.47	76.27
17	2	15	10	7	92.11	76.62
12	3	15	15	7	85.29	69.77
13	4	15	10	4	75.46	75.16
11	5	15	5	7	95.12	81.24
10	6	20	10	7	98.65	79.45
16	7	15	10	7	93.93	75.48
9	8	10	10	7	89.55	83.54
1	9	10	5	4	71.72	85.62
3	10	10	15	4	58.32	76.09
14	11	15	10	10	93.54	76.34
7	12	10	15	10	83.36	75.42
5	13	10	5	10	90.49	83.29
19	14	15	10	7	95.38	76.92
4	15	20	15	4	70.80	69.51
18	16	15	10	7	94.00	76.62
6	17	20	5	10	95.32	82.72
20	18	15	10	7	94.33	76.02
8	19	20	15	10	88.22	67.19
2	20	20	5	4	84.54	85.24

Quadratic RSM models for MB removal and membrane flux were both highly significant (F = 388.30 and 72.03, respectively; $p < 0.0001$; Table 7). The lack-of-fit tests were non-significant for MB removal (p = 0.9983) and flux (p = 0.0597), indicating no statistically detectable model inadequacy relative to pure error. The models showed strong fit and predictive performance: R^2 = 0.9971, adjusted R^2 = 0.9946, and predicted R^2 = 0.9956 for MB removal, and R^2 = 0.9848, adjusted R^2 = 0.9711, and predicted R^2 = 0.9036 for flux. The low CV values (0.89% and 1.12%) and adequate precision values of 73.13 and 28.30 further support the reliability of both models for prediction and optimization within the investigated ranges of factors.

Table 7 Summary of ANOVA analysis of dye removal and membrane flux

Response	Model *F*-value	Model *p*-value	Lack-of-fit *p*-value	R^2	Adjusted R^2	Predicted R^2
MB removal	388.3	< 0.0001	0.9983	0.9971	0.9946	0.9956
Membrane flux	72.03	< 0.0001	0.0597	0.9848	0.9711	0.9036

The regression model equations for dye removal and membrane flux are outlined in equations 11 and 12:

$$\textbf{MB dye removal}\ (\%) = \mathbf{94.01 + 4.41\,A - 5.12\,B + 9.01C - 0.0425\,AB - 1.95AC + 1.62\,BC - 0.0775\,A^2 - 3.97\,B^2 - 9.67\,C^2} \quad \text{Equation 11}$$

$$\textbf{Membrane Flux}\ \mathbf{Lm^2h^{-1} = 76.61 - 1.89\,A - 6.01\,B - 0.6665\,C - 1.74\,AB - 0.2306\,AC + 0.2312\,BC + 4.46\,A^2 - 1.53\,B^2 - 1.26\,C^2} \quad \text{Equation 12}$$

In the coded equations, *A*, *B*, and *C* represent filler loading, MB concentration, and solution pH, respectively. For MB removal, pH had the strongest positive linear effect (+9.01*C*), followed by filler loading (+4.41*A*), whereas increasing dye concentration reduced removal (-5.12*B*). This indicates that alkaline conditions and higher DIHYONE-CLI loading favored MB removal within the investigated range, whereas at higher dye concentrations, MB removal likely decreased due to saturation of available adsorption sites.

For membrane flux, dye concentration exerted the largest negative effect (-6.01*B*), followed by filler loading (-1.89*A*); pH had a smaller negative effect (-0.6665*C*). The flux reduction at higher dye concentration may reflect increased concentration polarization, dye accumulation, and transport resistance. Overall, the models reveal a removal-flux trade-off: higher filler loading and pH favored MB removal, whereas increasing dye concentration reduced both removal and flux. The models were therefore used for numerical optimization within the investigated ranges of factors. The developed models can therefore be used to identify operating conditions that maximize dye removal while maintaining acceptable membrane flux.

Fig. 14 compares the RSM-predicted responses with the corresponding experimental observations for MB removal and membrane flux. The data points cluster closely around the reference line for both responses, indicating good agreement between observed and model-predicted values (Abdulkadir et al., 2021; Ganesan & Begum, 2025; Javanmard et al., 2025). This graphical agreement is consistent with the high coefficients of determination obtained for MB removal (R^2 = 0.9971) and flux R^2 = 0.9848). The plot is a model-diagnostic result that evaluates prediction agreement for the CCD experimental runs, not only experiments conducted under optimized conditions.

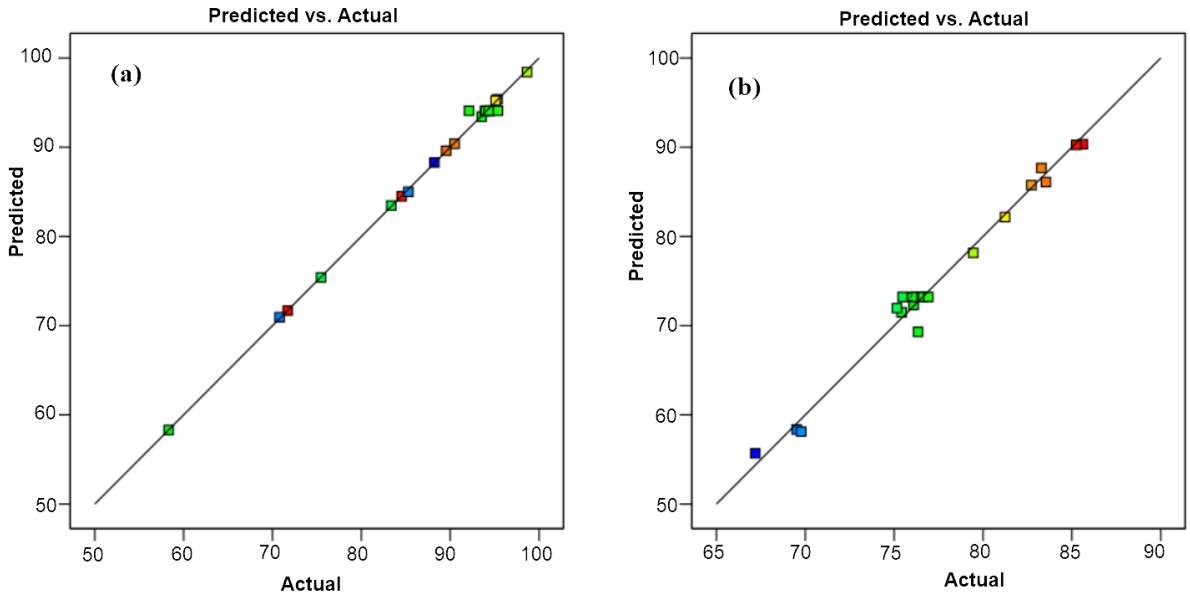


Fig. 14 Predicted and actual plots for (a) dye removal and (b) membrane flux.

The significant interaction surfaces are shown in Fig. 15. For MB removal, higher filler loading and lower dye concentration favored removal (Fig. 15a); this may be due to the availability of DIHYONE-CLI adsorption sites relative to the dye concentration. Removal also increased with pH, particularly at higher filler loading (Fig. 15b), although the negative AC (Equation 11) coefficient indicates that the combined benefit was less than purely additive. The dye concentration-pH surface (Fig. 15c) further shows that the highest removal occurred at low dye concentration and high pH, reflecting a favorable balance between available adsorption sites and the electrostatic attraction of cationic MB to the negatively charged filler surface.

For flux, the only significant interaction was between filler loading and dye concentration (Fig. 15d). Flux was highest at lower dye concentration and generally declined as dye concentration increased, with the magnitude of the decline dependent on filler loading. This behavior may be due to high concentration polarization, dye deposition, and transport resistance at higher dye concentration.

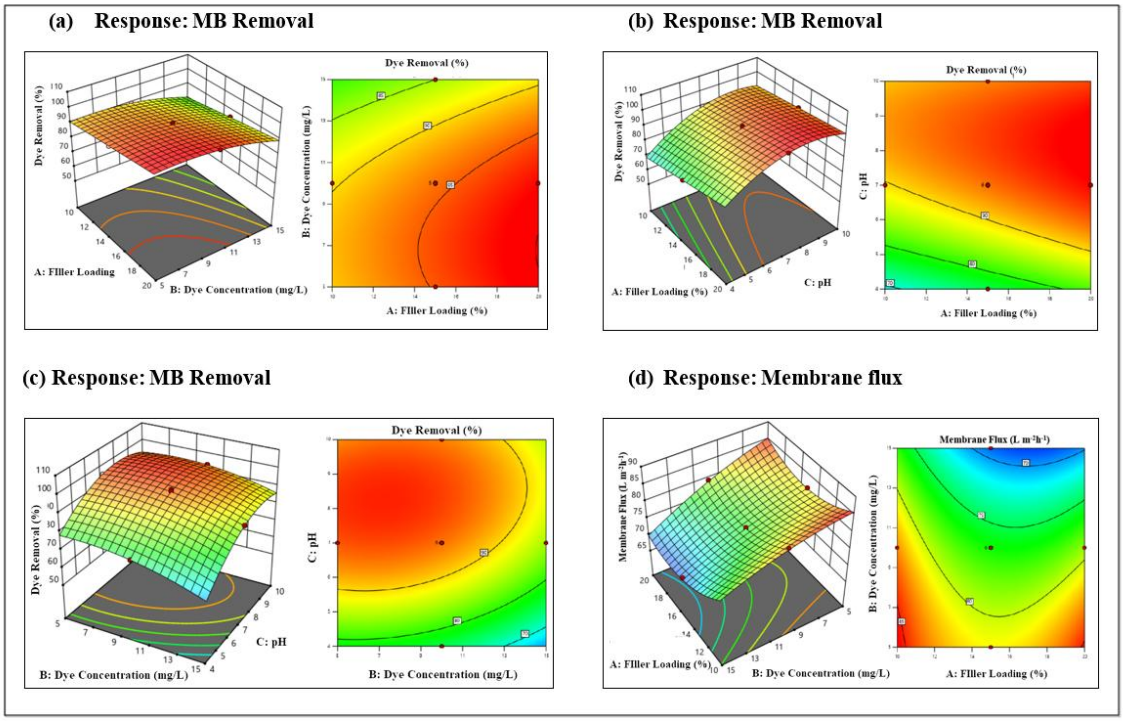


Fig. 15 2D and 3D plots for the effects of factors on dye removal (a, b, and c) and membrane flux (d) responses.

3.4.1 Optimization and validation of membrane filtration procedure

Numerical optimization of the fitted RSM models was performed in Design-Expert® using the desirability function to identify conditions that maximize MB removal while maintaining high membrane flux. In this approach, individual response desirability ranges from 0 (undesirable) to 1 (fully meeting the defined response goal), and the overall desirability is obtained by combining these individual response functions.

The optimal model-predicted condition was 20 wt.% filler loading, an initial MB concentration of 10.05 mg/L, and pH 8.46 (Table 8). Under these conditions, the models predicted MB removal of 99.52% and a membrane flux of

78.26 L $m^{-2}h^{-1}$. The overall desirability was 1.000, indicating that this solution satisfied the predefined optimization criteria for both responses. The predicted result is consistent with the response-surface analysis, which indicates that higher filler loading and an alkaline pH within the investigated range favored MB removal, while the selected intermediate dye concentration maintained an acceptable flux.

Table 8 Numerical optimization solution predicted by the RSM model

Parameter	**Optimized value**
Filler loading	20 wt.%
Initial MB concentration	10.05 mg/L
Solution pH	8.46
Predicted MB removal	99.52%
Predicted membrane flux	78.26 L $m^{-2}h^{-1}$
Overall desirability	1.000

Six independent confirmation experiments were conducted at the RSM-predicted optimum (20 wt.% DIHYONE-CLI, 10.05 mg L^{-1} MB, and pH 8.46). Experimental MB removal and flux ranged from 96.68- 98.66% and 73.97-77.68 L m^{-2} h^{-1}, respectively. The mean relative errors were 1.68% for MB removal and 3.16% for flux, with all individual errors below 6% (Table 9). These results support the predictive reliability of the RSM models (Mutalib et al., 2025). These validation results support the adequacy of the developed RSM models in predicting MB removal and flux within the investigated ranges of factors.

Table 9 Predicted and actual values for dye removal and membrane flux under optimized conditions

Run	MB removal			Flux		
	Actual (%)	Predicted (%)	Error (%)	Actual (L $m^{-2}h^{-1}$)	Predicted (L $m^{-2}h^{-1}$)	Error (%)
1	98.64	99.52	0.88	76.04	78.26	2.84
2	96.68	99.52	2.85	76.43	78.26	2.34
	98.66	99.52	0.86	73.97	78.26	5.48
4	97.94	99.52	1.59	77.68	78.26	0.74
5	98.54	99.52	0.98	76.19	78.26	2.65
6	96.83	99.52	2.7	74.99	78.26	4.18
Mean relative error			**1.68**			**3.16**

3.5 Reusability test of the membrane

The reusability of the optimized 20 wt.% DIHYONE-CLI/PES membrane was evaluated through five consecutive methylene blue (MB) filtration-regeneration cycles. In each cycle, a 10 mg/L MB solution was filtered, after which the membrane was regenerated by hydraulic cleaning with 2% (w/v) $CaCl_2$ solution in 30:70 ethanol/water for 30 min before reuse. As shown in Fig. 16, the membrane retained high MB removal during repeated use. Removal decreased gradually from 97.71% in the first cycle to 87.54% in the fifth cycle, corresponding to a 10.41% relative loss and retention of 89.59% of the initial removal performance. Flux declined from 67.93 to 57.91 L $m^{-2}h^{-1}$ over the same period, corresponding to a 14.75% reduction and retention of 85.25% of the initial flux. The most noticeable decrease occurred after the third cycle.

The progressive decline in removal and flux may reflect incomplete MB desorption during regeneration, resulting in residual dye at accessible filler sites or within membrane pores. Residual dye can reduce the number of available adsorption sites and increase hydraulic resistance through partial pore constriction. Overall, retention of 87.54% MB removal and 85.25% flux after five cycles demonstrates that the optimized membrane has good short-term regeneration stability under the applied cleaning procedure.

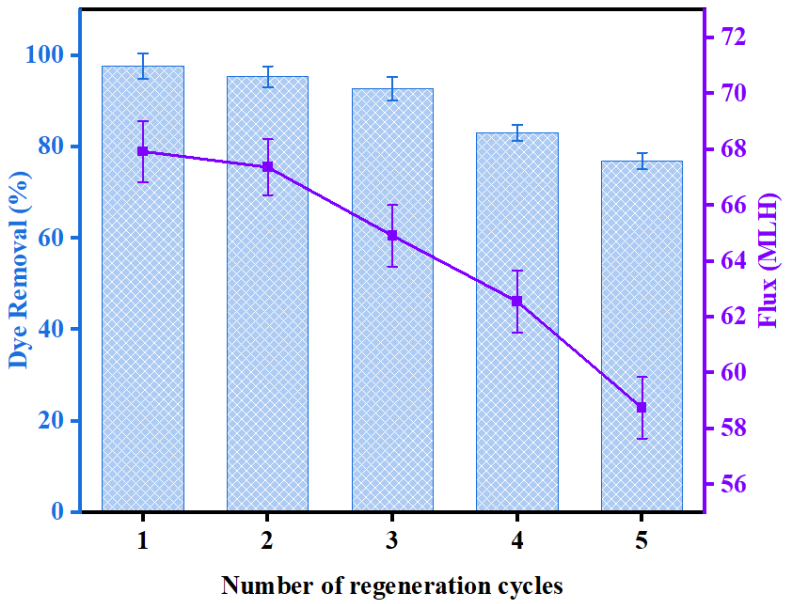


Fig. 16 Regeneration cycles of the 20 wt.% DIHYONE-CLI/PES membrane

3.6 Proposed Interfacial and Adsorption Mechanisms of the DIHYONE-CLI/PES Mixed-Matrix Membrane

Fig. 17 (a) illustrates the proposed interfacial interactions between DIHYONE-functionalized clinoptilolite (DIHYONE-CLI) and the PES matrix. DIHYONE functionalization introduces organosilane-linked aromatic and polar groups onto clinoptilolite, improving its compatibility with aromatic PES. The modified filler may associate with PES through π-π interactions between aromatic moieties and hydrogen bonding between DIHYONE hydroxyl groups and PES sulfone oxygens (Han et al., 2019). The combined non-covalent interactions may improve filler-polymer adhesion, promote more uniform filler dispersion, and reduce the formation of non-selective interfacial voids or filler agglomerates during phase inversion.

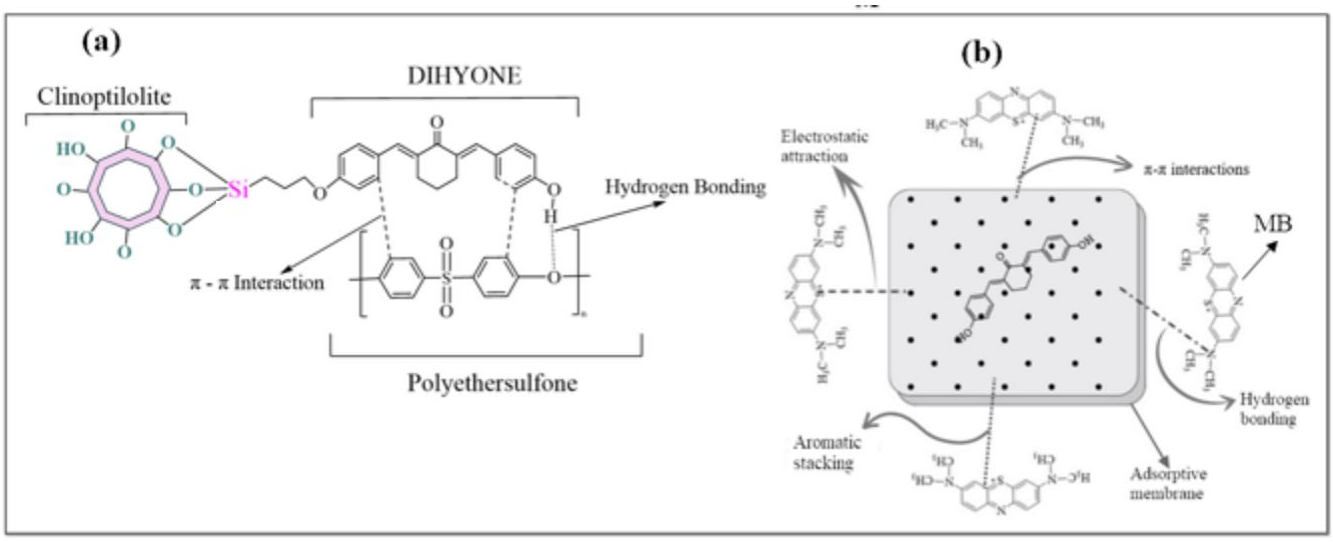


Fig. 17 Proposed **(a)** non-covalent interfacial interactions between DIHYONE–CLI and the PES matrix; and **(b)** adsorption mechanism of methylene blue (MB) by DIHYONE–CLI/PES membrane

Beyond improving filler-polymer compatibility, DIHYONE functionalization may introduce accessible sites that contribute to methylene blue (MB) removal (Bahmanzadegan & Ghaemi, 2024b). As illustrated in Fig. 12(b), the aromatic domains of DIHYONE-CLI may interact with the conjugated aromatic structure of MB through π-π interactions. Polar groups on the DIHYONE-functionalized filler may also participate in hydrogen-bonding interactions with heteroatom groups in MB (Aisha et al., 2026). In addition, the negatively charged aluminosilicate framework of clinoptilolite is expected to promote electrostatic attraction of cationic MB, particularly under the higher-pH conditions associated with greater removal in the RSM analysis.

3.7 Comparison of reported membranes' performance for MB removal

Table 10 compares the MB-removal performance of the DIHYONE–CLI/PES membrane with selected membranes reported in the literature. Under the optimized conditions of this study, DIHYONE–CLI/PES achieved 98.63% MB removal with a flux of 76.04 L $m^{-2}h^{-1}$. This removal was comparable to CA/ZIF-8/GO (99.7%) and mercapto-zeolite/PVDF (97.01%), while providing a higher flux than mercapto-zeolite/PVDF (37.14 L $m^{-2}h^{-1}$) and PES/POM–TiO_2 (35.9 s. The GO-HBE/PES membrane exhibited a higher flux (200 L $m^{-2}h^{-1}$) but lower MB removal (85.9%),

illustrating the common permeability-removal trade-off. These results indicate that DIHYONE–CLI/PES provides a competitive balance between MB removal and permeate flux.

Table 10 Comparative summary of the performance of DIHYONE-CLI and membranes for MB removal

Membrane	**Removal (%)**	**Flux (**L $m^{-2}h^{-1}$**)**	**Additive amount/wt.%**	**Reference**
CA/ZIF-8/GO	99.7	83.92	10/5	(Sutrisna et al., 2026)
PES/POM-TiO_2	90 (uv)	35.9	0.5	(Zhafiri et al., 2023)
Mercapto-zeolites/PVDF	97.01	37.14	0.75	(Kadja et al., 2023)
GO-HBE/PES	85.9	200	5	(Mahmoudian & Kochameshki, 2021)
PES/CNF	69.17	86.78	2	(Ng et al., 2020)
DIHYONE-CLI/PES	98.63	76.04	20	This study

4.0 Conclusion

This study developed a DIHYONE-functionalized clinoptilolite (DIHYONE–CLI) hybrid filler for incorporation into polyethersulfone (PES) mixed-matrix membranes. FTIR, XRD, SEM–EDX, TGA, BET, and zeta-potential analyses supported successful modification and characterization of the hybrid filler. However, the proposed interfacial bonding configuration requires further confirmation by surface-sensitive techniques, such as X-ray photoelectron spectroscopy (XPS). Incorporation of DIHYONE–CLI influenced membrane structure and performance, with moderate filler loading providing the most favorable balance between dye removal and water transport. The filler-modified membranes retained a finger-like porous substructure, although excessive loading caused a reduction in porosity and could increase transport resistance.

RSM identified filler loading, initial MB concentration, and solution pH as significant factors governing MB removal and membrane flux. The numerical optimum within the tested domain was 20 wt.% DIHYONE–CLI, an

MB concentration of 10.05 mg/L, and pH 8.46. At these conditions, the model predicted 99.52% MB removal and 78.26 L $m^{-2}h^{-1}$ flux. Six confirmatory experiments yielded average relative errors of approximately 1.6% for MB removal and 3.0% for flux, supporting the predictive adequacy of the RSM models. The optimized membrane also exhibited short-term regeneration stability. After five filtration–regeneration cycles using 30% ethanolic $CaCl_2$, it retained 87.54% MB removal and 85.25% of its initial flux. The results therefore demonstrate the potential of DIHYONE-CLI/PES membranes for MB removal under the studied conditions. Further work should evaluate long-term cycling, filler or modifier leaching, membrane performance with mixed dyes and real wastewater, and post-filtration surface characterization.

5.0 Acknowledgement

This research was funded by the Ministry of Higher Education, Malaysia under Fundamental Research Grant Scheme (Grant Number: FRGS/1/2024/TK05/USM/02/2), Universiti Sains Malaysia through grants obtained under the Research University Transdisciplinary (RUTrans) Grant Scheme (Grant Number: R502-KR-RUT002-0000001109-K134) and the Internationalization Incentive Scheme provided (Grant Number: R502-KR-ARP004-00AUPRM003-K134). Furthermore, the authors would like to express their gratitude to the School of Chemical Sciences and the Research Creativity and Management Office (RCMO) of Universiti Sains Malaysia for their invaluable technical support.

Statements and Declarations

The authors have no competing interests to declare that are relevant to the content of this article.

Data Availability

The datasets used during this study are available from the corresponding author on request.

6.0 References

Abdulkadir, I., Mohammed, B. S., Liew, M. S., & Wahab, M. M. A. (2021). Modelling and Optimization of the Mechanical Properties of Engineered Cementitious Composite Containing Crumb Rubber Pretreated With

Graphene Oxide Using Response Surface Methodology. *Construction and Building Materials*, *310*, 125259. https://doi.org/10.1016/j.conbuildmat.2021.125259

Abubakar, S., Khairuddean, M., Ismail, N. Z., Salhimi, S. M., Al-Amin, M., & Wahyuningsih, T. D. (2024). Synthesis and computational insights of hybrid heterocyclic bis-chalcone compounds and their cytotoxic effects against breast cancer cells. *Results in Chemistry*, *7*. https://doi.org/10.1016/j.rechem.2024.101464

Ahmadi, B., Fallah, A., Ghamarpoor, R., & Jamshidi, M. (2025). Methylene blue beyond the dye: A critical review on its role as a benchmark pollutant in photocatalyst design. *Results in Chemistry*, *18*, 102910. https://doi.org/https://doi.org/10.1016/j.rechem.2025.102910

Aisha, N., Nurbanu, S., Seitkan, A., Raikhan, R., Yermakhanov, M., Gaukhar, T., Gulsim, M., Gaukhar, Z., Olzhas, N., & Ergali, R. (2026). Zeolite-Based Composite Nanomaterials for Organic Micropollutant Removal: Structure–Property–Performance Relationships and Practical Challenges. *Nanomaterials*, *16*(10). https://doi.org/10.3390/nano16100635

Akyalcin, S., Akar, C., Yaman, A., Tamer, M., & Akyalcin, L. (2026). Modified Clinoptilolite Zeolites as Heterogeneous Catalysts for Bio-oil Upgrading via Esterification of Acetic Acid with n-butanol. *ChemistrySelect*, *11*(6), e05028. https://doi.org/https://doi.org/10.1002/slct.202505028

Almansouri, H. E., Edokali, M., & Seman, M. N. A. (2024). Flat Sheet Thin Film Composite Forward Osmosis Membranes for Water Treatment and Purification: A Review on Modification Techniques and Concepts. *Desalination and Water Treatment*, *320*, 100815. https://doi.org/10.1016/j.dwt.2024.100815

Alsuhybani, M., Alshehri, S., Alquwaizany, A., Alosime, E., Alaeq, R., & Alrehaili, A. (2026). Effective adsorption of methylene blue using natural Saudi zeolite as a low-cost sustainable adsorbent. *Scientific Reports*, *16*(1), 211. https://doi.org/10.1038/s41598-025-33491-9

Ambrožová, P., Kynický, J., Urubek, T., & Nguyen, V. (2017). Synthesis and Modification of Clinoptilolite. *Molecules*, *22*(7), 1107. https://doi.org/10.3390/molecules22071107

Anbealagan, L. D., Ng, T. Y. S., Chew, T. L., Yeong, Y. F., Low, S. C., Ong, Y. T., Ho, C., & Jawad, Z. A. (2021). Modified Zeolite/Polysulfone Mixed Matrix Membrane for Enhanced CO2/CH4 Separation. *Membranes*, *11*(8), 630. https://doi.org/10.3390/membranes11080630

Babapour, A., & Şen, M. (2024). Effect of Silica Type, Content, and Silanization on the Curing, Mechanical and Energy Dissipation Properties of Poly (Epichlorohydrin-Co-Ethylene Oxide-Co-Allyl Glycidyl Ether) Elastomers. *European Polymer Journal*, *206*, 112774. https://doi.org/10.1016/j.eurpolymj.2024.112774

Bahmanzadegan, F., & Ghaemi, A. (2024a). Modification and Functionalization of Zeolites to Improve the Efficiency of CO2 Adsorption: A Review. *Case Studies in Chemical and Environmental Engineering*, *9*, 100564. https://doi.org/10.1016/j.cscee.2023.100564

Bahmanzadegan, F., & Ghaemi, A. (2024b). Modification and functionalization of zeolites to improve the efficiency of CO2 adsorption: A review. *Case Studies in Chemical and Environmental Engineering*, *9*, 100564. https://doi.org/https://doi.org/10.1016/j.cscee.2023.100564

Bessegato, G. G., Brugnera, M. F., & Zanoni, M. V. B. (2019). Electroanalytical sensing of dyes and colorants. *Current Opinion in Electrochemistry*, *16*, 134–142. https://doi.org/https://doi.org/10.1016/j.coelec.2019.05.008

Bhiogade, A., & Kannan, M. (2021). Studies on thermal and degradation kinetics of cellulose micro/nanoparticle filled polylactic acid (PLA) based nanocomposites. *Polymers and Polymer Composites*, *29*(9), S85–S98. https://doi.org/10.1177/0967391120987170

Cadar, O., Senila, M., Hoaghia, M. A., Scurtu, D., Miu, I., & Levei, E. A. (2020). Effects of thermal treatment on natural clinoptilolite-rich zeolite behavior in simulated biological fluids. *Molecules*, *25*(11). https://doi.org/10.3390/molecules25112570

Cechinel, M. A. P., Mayer, D. A., Pozdniakova, T. A., Mazur, L. P., Boaventura, R. A. R., de Souza, A. A. U., de Souza, S. M. A. G. U., & Vilar, V. J. P. (2016). Removal of metal ions from a petrochemical wastewater using brown macro-algae as natural cation-exchangers. *Chemical Engineering Journal*, *286*, 1–15. https://doi.org/10.1016/j.cej.2015.10.042

Chen, X., Zhang, T., Sun, P., Yu, F., Li, B., & Dun, L. (2022). Application of Organic Amine Modified Natural Zeolite in Filling Natural Rubber. *Nanomaterials*, *12*(16), 2784. https://doi.org/10.3390/nano12162784

de Lima, R. C. F., da Silva Oliveira, D., & Pergher, S. B. C. (2021). Interzeolitic transformation of clinoptilolite into gis and lta zeolite. *Minerals*, *11*(12). https://doi.org/10.3390/min11121313

Dikić, J., Stojakovic, D., Rajic, N., Pavlovic, J., & Milenkovic, J. (2013). *SURFACE MODIFICATION OF THE NATURAL CLINOPTILOLITE FOR ITS POTENTIAL USE FOR THE NITRATE REMOVAL FROM WATER MEDIA*. https://www.researchgate.net/publication/313860600

Dimitrijević, J., Petrović, J., Marinković, A., Dikić, J., Koprivica, M., Simić, M., & Jevtić, S. (2025). Preparation, characterization, adsorption, and antibacterial assessments of silane-functionalized zeolites. *Macedonian Journal of Chemistry and Chemical Engineering*, *44*(2). https://doi.org/10.20450/mjcce.2025.3103

Dionisiou, N. S., & Matsi, T. (2024). *Natural and Surfactant-Modified Zeolite for the Removal of Pollutants (Inorganic Mainly) From Natural Waters and Wastewaters*. 545–570. https://doi.org/10.1016/b978-0-443-22069-2.00026-7

Fitri, A., Prasetya, B., Aini, Q., Ikhsan, F., Aflaha, R., Triyana, K., Taher, T., Arif, M. F., & Rianjanu, A. (2025). Enhanced Methylene Blue Adsorption Capacity of 3d-Printed Zeolite/Glycerol (3d-Ze/Gy) by Sintering Temperature Optimalizations. *Next Materials*, *9*, 101069. https://doi.org/10.1016/j.nxmate.2025.101069

Ganesan, V., & Begum, K. M. M. S. (2025). Exploratory Electrosorption Performance of Dual Chambered Cylindrical Flow Through System: A Response Surface Approach. *Chemical Engineering Research and Design*, *220*, 635–651. https://doi.org/10.1016/j.cherd.2025.07.043

Grifasi, N., Ziantoni, B., Mondello, A., Cruciani, G., Rizzetto, A., Lavagna, L., Pavese, M., Deorsola, F. A., Fino, D., & Piumetti, M. (2026). Natural zeolite clinoptilolite for sustainable energy applications: Insights into water affinity and adsorption properties. *Journal of Energy Storage*, *179*, 123782. https://doi.org/https://doi.org/10.1016/j.est.2026.123782

Han, X., Wu, L., Zhang, H., He, A., & Nie, H. (2019). Inorganic–Organic Hybrid Janus Fillers for Improving the Thermal Conductivity of Polymer Composites. *ACS Applied Materials & Interfaces*, *11*(13), 12190–12194. https://doi.org/10.1021/acsami.8b22278

Han, X., Yu, J., Cao, Z., Wang, R., Du, W., He, P., & Ge, Y. (2020). Preparation and Properties of Silane Coupling Agent Modified Zeolite as Warm Mix Additive. *Construction and Building Materials*, *244*, 118408. https://doi.org/10.1016/j.conbuildmat.2020.118408

Hashmi, S. A. M., Hussain, W., Bhanbhro, H., Anggraini, L., & Ismail, M. (2026). Zeolites in membrane technology: A review of interface design, computational modeling, predictive framework and future engineering directions. *Journal of Environmental Chemical Engineering*, *14*(5), 123746. https://doi.org/https://doi.org/10.1016/j.jece.2026.123746

Imron, M. F., Kurniawan, S. B., Soegianto, A., & Wahyudianto, F. E. (2019). Phytoremediation of methylene blue using duckweed (Lemna minor). *Heliyon*, *5*(8). https://doi.org/10.1016/j.heliyon.2019.e02206

Irma, M., Foo, K. Y., Susilawati, S., Yusof, E. N. M., Nishiyama, N., & Sabar, S. (2025). Advancements in Zeolite and Zeolite-Based Sorbents: Modification Strategies in Mitigating Nitrogen-Containing Pollutants From Water and Wastewater. *Inorganic Chemistry Communications*, *172*, 113715. https://doi.org/10.1016/j.inoche.2024.113715

Javanmard, A., Daud, W. M. A. W., Patah, M. F. A., & Zuki, F. M. (2025). An Innovative Method for Optimizing Continuous Torrefaction in a Helical Screw-Induced Rotational Fluidised Bed Reactor: Merging Flow Dynamics, Energy Efficiency, and Biomass Pretreatment to Augment Biochar Production. *Chemical Engineering Journal*, *525*, 169851. https://doi.org/10.1016/j.cej.2025.169851

Jusoh, N., Yeong, Y. F., Lau, K. K., & Shariff, A. M. (2018). Effects of amine-functionalization on mixed matrix membranes encompassing of T-type zeolite and 6FDA-based polyimide for separation of CO2 from CH4. *International Journal of Automotive and Mechanical Engineering*, *15*(1), 5126–5134. https://doi.org/10.15282/ijame.15.1.2018.17.0396

Kadja, G. T. M., Dwihermiati, E., Sagita, F., Mukhoibibah, K., Umam, K., Ledyastuti, M., & Radiman, C. L. (2023). Mercapto Functionalized–natural Zeolites/PVDF Mixed Matrix Membrane for Enhanced Removal of Methylene Blue. *Inorganic Chemistry Communications*, *157*, 111263. https://doi.org/10.1016/j.inoche.2023.111263

Khan, Z. I., Mohsin, M. E. A., Habib, U., Mousa, S., Hossain, S. K. S., Ali, S. S., Mohamad, Z., & Othman, N. (2025). Enhanced Mechanical and Thermal Performance of Sustainable RPET/PA-11/Joncryl® Nanocomposites Reinforced with Halloysite Nanotubes. *Polymers*, *17*(11). https://doi.org/10.3390/polym17111433

Król, M., Dechnik, J., Szymczak, P., Handke, B., Szumera, M., & Stoch, L. (2024). Thermal Behavior of Clinoptilolite. *Crystals*, *14*(7), 646. https://doi.org/10.3390/cryst14070646

Li, H., Feng, Y., Li, J., & Yang, Y. (2025). Enhancing Interfacial Compatibility of PIM-1-Based Mixed-Matrix Membranes through In Situ-Formed cPIM-1 Networked Fillers. *ACS Sustainable Chemistry & Engineering*, *13*(48), 20893–20905. https://doi.org/10.1021/acssuschemeng.5c09984

Lu, S., Xue, W., Wang, H., Liu, Q., Han, R., & Mei, D. (2023). A Surface-Induced Coating Strategy for Constructing Hydrophobic Zeolite Composite to Enhance the Toluene Adsorption in Humid Environment. *Chemical Engineering Journal*, *471*, 144570. https://doi.org/10.1016/j.cej.2023.144570

Mahmoudian, M., & Kochameshki, M. G. (2021). The Performance of Polyethersulfone Nanocomposite Membrane in the Removal of Industrial Dyes. *Polymer*, *224*, 123693. https://doi.org/10.1016/j.polymer.2021.123693

Męczyńska-Wielgosz, S., Piotrowska, A., Majkowska-Pilip, A., Bilewicz, A., & Kruszewski, M. (2016). Effect of Surface Functionalization on the Cellular Uptake and Toxicity of Nanozeolite A. *Nanoscale Research Letters*, *11*(1). https://doi.org/10.1186/s11671-016-1334-8

Mortazavi, N., Bahadori, M., Marandi, A., Tangestaninejad, S., Moghadam, M., Mirkhani, V., & Mohammadpoor-Baltork, I. (2021). Enhancement of CO2 adsorption on natural zeolite, modified clinoptilolite with cations, amines and ionic liquids. *Sustainable Chemistry and Pharmacy*, *22*. https://doi.org/10.1016/j.scp.2021.100495

Mutalib, N. F. A. A., Seitkhan, A., Othman, M. B. H., Ramle, A. Q., Salleh, N. M., Othman, M. H. D., Hubadillah, S. K., Jamalludin, M. R., Yusof, N. N., & Adam, M. R. (2025). Revolutionizing dye removal in wastewater: An optimization study of curcumin-functionalized zeolite beads for methylene blue adsorption. *Surfaces and Interfaces*, *72*. https://doi.org/10.1016/j.surfin.2025.107434

Naito, M., Yokoyama, T., Hosokawa, K., & Nogi, K. (Eds.). (2018). Chapter 2 - Structural Control of Nanoparticles. In *Nanoparticle Technology Handbook (Third Edition)* (pp. 49–107). Elsevier. https://doi.org/https://doi.org/10.1016/B978-0-444-64110-6.00002-0

Ng, C. Y., Khoo, L. H., Ng, L. Y., Ong, C. B., Mahmoudi, E., Rohani, R., & Mohammad, A. W. (2020). Novel Polyethersulfone-Cellulose Composite Thin Film Using Sustainable Empty Fruit Bunches From Elaeis Guineensis for Methylene Blue Removal. *Polymer Testing*, *86*, 106494. https://doi.org/10.1016/j.polymertesting.2020.106494

Nizam, M. K., Azhari, S., & Tamar Jaya, M. A. (2021). Modified Zeolite as Purification Material in Wastewater Treatment: A Review. *Scientific Research Journal*, *18*(2), 177–213. https://doi.org/10.24191/srj.v18i2.12092

Özel, C., Akat, C., Alosmanov, R., Kahveci, M. U., Emir, C., & Yücel, S. (2021). Surface modification of zeolite and kaolin with 3-(aminopropyl) triethoxysilane and 3-(trimethoxysilyl) propyl methacrylate. *Bulgarian Chemical Communications*, *53*(4), 464–470. https://doi.org/10.34049/bcc.53.4.T003

Pakharuddin, N. H., Fazly, M. N., Ahmad Sukari, S. H., Tho, K., & Zamri, W. F. H. (2021). Water treatment process using conventional and advanced methods: A comparative study of Malaysia and selected countries. *IOP Conference Series: Earth and Environmental Science*, *880*(1), 012017. https://doi.org/10.1088/1755-1315/880/1/012017

Postole, G., Segondy, S., Cabanis, T., Nguyen, T.-H., Auroux, A., & Dubois, J.-L. (2025). Relationship Between Number and Strength of Acid–Base Catalytic Sites and Their Performances in Isopropanol Dehydration Reaction. *Catalysts*, *15*(8). https://doi.org/10.3390/catal15080768

Rafiee, E. (2025). Powering the Future: Emerging Role and Mechanistic Insights of Polyoxometalates in Piezo- And Triboelectric Energy Materials. *RSC Advances*, *15*(49), 42192–42209. https://doi.org/10.1039/d5ra06465a

Rathi, B. S., Kumar, P. S., & Show, P. L. (2021). A Review on Effective Removal of Emerging Contaminants From Aquatic Systems: Current Trends and Scope for Further Research. *Journal of Hazardous Materials*, *409*, 124413. https://doi.org/10.1016/j.jhazmat.2020.124413

Restiawaty, E., Gozali, V. A., Wibisono, T. A. S. E., & Budhi, Y. W. (2024). Utilizing Modified Clinoptilolite for the Adsorption of Heavy Metal Ions in Acid Mine Drainage. *Case Studies in Chemical and Environmental Engineering*, *9*, 100706. https://doi.org/10.1016/j.cscee.2024.100706

Russo, F., Bulzomì, M., Nicolò, E. Di, Ursino, C., & Figoli, A. (2021). Enhanced Anti-Fouling Behavior and Performance of PES Membrane by UV Treatment. *Processes*, *9*(2), 246. https://doi.org/10.3390/pr9020246

Sáez, P., Rodríguez, A., Gómez, J. M. G., Paramio, C., Fraile, C. D. S., & Díez, E. (2021). H-Clinoptilolite as an Efficient and Low-Cost Adsorbent for Batch and Continuous Gallium Removal From Aqueous Solutions. *Journal of Sustainable Metallurgy*, *7*(4), 1699–1716. https://doi.org/10.1007/s40831-021-00437-0

Saheed, M., Shama, U. B., Lami, A. K., Shaba, E. Y., Obayomi, K. S., Babajide, A. O., Tijani, J. O., Abdulkareem, A. S., & Ndamitso, M. M. (2026). Polymeric membrane technologies for wastewater treatment and valorization: Advancing sustainable and circular water systems. *Journal of Environmental Sciences*, 105674. https://doi.org/https://doi.org/10.1016/j.jes.2026.105674

Samanta, N. S., Mondal, P., Dhara, S., Bora, U., & Purkait, M. K. (2023). Fabrication of LD-slag Derived Zeolite Y Coated Polysulfone (PSf) Membrane for Decontamination of Groundwater. *Chemical Engineering Journal*, *478*, 147330. https://doi.org/10.1016/j.cej.2023.147330

Shi, Y., Wang, X., Feng, C., Chen, W., & Yang, S. (2023). Adsorption Properties of Natural Zeolite Supported by Chitosan on Cd(II) in Micropolluted Irrigation Water. *Acs Omega*, *9*(1), 573–584. https://doi.org/10.1021/acsomega.3c06041

Song, S., Li, H., Li, J., & Yang, Y. (2025). Enhancing interfacial compatibility of porous organic polymer-filled mixed-matrix membranes using covalent grafted PIM-1 network. *Separation and Purification Technology*, *354*, 129442. https://doi.org/https://doi.org/10.1016/j.seppur.2024.129442

Sutrisna, P. D., Mustika, P. C. B. W., Wijaya, C., Sutama Putra, V. I. W., Denaswara, P. D. D., Hadi, R. P., Widianto, A. Y., & Purwanto, E. (2026). Synergistic effects of combining ZIF-8 and graphene oxide inside cellulose acetate-based mixed matrix membranes on the removal of methylene blue. *Case Studies in Chemical and Environmental Engineering*, *13*, 101338. https://doi.org/https://doi.org/10.1016/j.cscee.2026.101338

Tayeh, Y. A., Alazaiza, M. Y. D., Al-Zghoul, T. M., & Bashir, M. J. K. (2025). A Comprehensive Review of RO Membrane Fouling: Mechanisms, Categories, Cleaning Methods and Pretreatment Technologies. *Journal of Hazardous Materials Advances*, *18*, 100684. https://doi.org/10.1016/j.hazadv.2025.100684

Tian, C., Feng, Y., Chu, G., Lu, Y., Miao, C., Ning, N., Zhang, L., & Tian, M. (2020). Interfacial Nanomechanical Properties and Chain Segment Dynamics of Fibrillar Silicate/Elastomer Nanocomposites. *Composites Part B Engineering*, *193*, 108048. https://doi.org/10.1016/j.compositesb.2020.108048

Wang, C., Leng, S., Xu, Y., Tian, Q., Zhang, X., Cao, L., & Huang, J. (2018). Preparation of amino functionalized hydrophobic zeolite and its adsorption properties for chromate and naphthalene. *Minerals*, *8*(4). https://doi.org/10.3390/min8040145

Wang, C., Wang, L., Du, F., Yu, Q., & Liang, X. (2023). A two-step organic modification strategy for improving surface hydrophobicity of zeolites. *Advanced Powder Technology*, *34*(11), 104228. https://doi.org/https://doi.org/10.1016/j.apt.2023.104228

Zare, Y. (2016). Study of Nanoparticles Aggregation/Agglomeration in Polymer Particulate Nanocomposites by Mechanical Properties. *Composites Part a Applied Science and Manufacturing*, *84*, 158–164. https://doi.org/10.1016/j.compositesa.2016.01.020

Zhafiri, S., Ali, B. T. I., Gunawan, T., & Widiastuti, N. (2023). Fabrication of PES/POM-TiO2 Mixed Matrix Membrane With Photocatalytic Activity for Methylene Blue Removal. *Materials Today Proceedings*, *74*, 471–475. https://doi.org/10.1016/j.matpr.2022.11.256

Supplementary Files

This is a list of supplementary files associated with this preprint. Click to download.

- SupplementaryInformation1.docx